

**Non-destructive observation of morphological
and structural alterations in industrial
materials based on near-infrared
spectral-domain optical coherence tomography**

Department of Bio-Functions and System Science
Graduate School of Bio-Applications and Systems Engineering
Tokyo University of Agriculture and Technology

Takeshi Makino

Table of contents

Chapter 1 Introduction.....	1
1.1 Introduction Remark.....	1
1.2 Synopsis of the Dissertation.....	10
 Chapter 2 Principles of Optical Coherence Tomographic Imaging.....	 12
2.1 Basic concept of Optical Coherence Tomography (OCT)	12
2.2 Laser Michelson Interferometer.....	13
2.3 Time-domain Optical Coherence Tomography (TD-OCT)	20
2.4 Spectral-domain Optical Coherence Tomography (SD-OCT)	22
2.5 Time-Stretch Spectral-domain Optical Coherence Tomography (TS SD-OCT)	 27
2.6 Conclusions.....	31
 Chapter 3 Evaluation of Attenuation Coefficient using Optical Coherence Tomography.....	 32
3.1 Induction.....	32
3.2 Definitions of Attenuation Coefficient in OCT measurement	34
3.3 Experimental Setup and Procedures	37
3.4 Experiment and Discussion.....	40
3.5 Conclusions.....	43

Chapter 4 Analysis of Natural Water Evaporation Process using

Dual-wavelength Optical Coherence Tomography

in Spectral Domain.....	44
4.1 Introduction.....	44
4.2 Experimental Setup and Samples.....	47
4.2.1 Two-wavelength OCT System in Spectral Domain	47
4.2.2 Samples used in the Experiment.....	50
4.3 Numerical Procedures of Quantitative Analysis.....	54
4.4. Experimental Results and Discussions.....	56
4.4.1 Water Distribution Imaging Inside Celery.....	56
4.4.2 Water Distribution Imaging Inside Sheet of Compressed Dry Leaves.....	61
4.5 Conclusions.....	68

Chapter 5 Analysis of Water Evaporation Process by Temperature

Control System for Peltier Element using Near-infrared Optical

Coherence Tomography in Spectral domain.....	70
5.1 Induction.....	70
5.2 Experimental Setup and Samples.....	71
5.2.1 Real-time Near-infrared SD-OCT System.....	71
5.2.2 Sheet of Compressed Dry Leaves and Evaporation Process.....	74
5.3 Experimental Results and Discussions.....	77
5.3.1 Evaporation Process over Time in Natural Drying.....	77

5.3.2 Evaporation Process over Time in the Short-Time Drying using the Heating-system.....	83
5.4 Conclusions.....	88
 Chapter 6 Development of Faster SD-OCT System using Time-Stretch Spectroscopy.....	 89
6.1 Induction.....	89
6.2 Procedure for calculating the distance using the approximation method.....	91
6.3 Experimental setup and method.....	94
6.4 Experimental Result and Discussions.....	96
6.5 Conclusion.....	102
 Chapter 7 Conclusions.....	 103
 References	 106
 Acknowledgment	 114

Chapter 1

Introduction

1.1 Introduction Remark

In recent years, optical coherence tomography (OCT) has been developed as a method for obtaining tomographic images of industrial materials. This is a tomographic imaging method that uses optical interference in the near-infrared wavelength band. As the spatial resolution is approximately 1–10 μm , micro-tomographic images of morphological and structural alterations can be obtained. In addition, it is a safe and simple system with non-destructive characteristics. Thus, using this OCT technique, information on biological activity can be acquired in the living tissue, while morphological alterations with high accuracy can be acquired in the industrial field. In plants, water typically comprises 70–95% of the biomass of nonwoody tissues such as leaves and roots. At the cellular level, water is the primary medium used to transport metabolites through the cell, whereas at the whole-plant level, it is responsible for transporting the raw materials from one plant organ to another. These movements through water are caused by the absorption and evaporation of water from the roots and plant leaves, respectively, and observing the water state of the leaves is crucial [1]. Water movement is important for plant physiology, and studies have analyzed biological activity by imaging water in living plants [2]. As a method of imaging water on the surface of the biological tissues, the methods using high frequency current [3], attenuated total reflectance Fourier transform infrared (ATR-FTIR) [4], and in vivo confocal Raman spectroscopy (CRS) [5-6] have been proposed. Further, as an internal measurement, the methods using ultrasound, computed tomography (CT),

and magnetic resonance imaging (MRI) have been used in the medical field. OCT has been used for imaging the tissue distribution localized in biological tissue at a depth of approximately 1 mm. A comparison of the OCT level with other similar methods is shown in Fig. 1.1 [7]. Compared with MRI and ultrasonography, OCT offers a limited imaging area in terms of depth of the object to be measured; however, it has a high resolution. In addition, OCT is a tomographic imaging method that employs optical coherence, and high-resolution imaging of tissue distribution in the biological tissue can be performed through non-contact and noninvasive measurements [8-10].

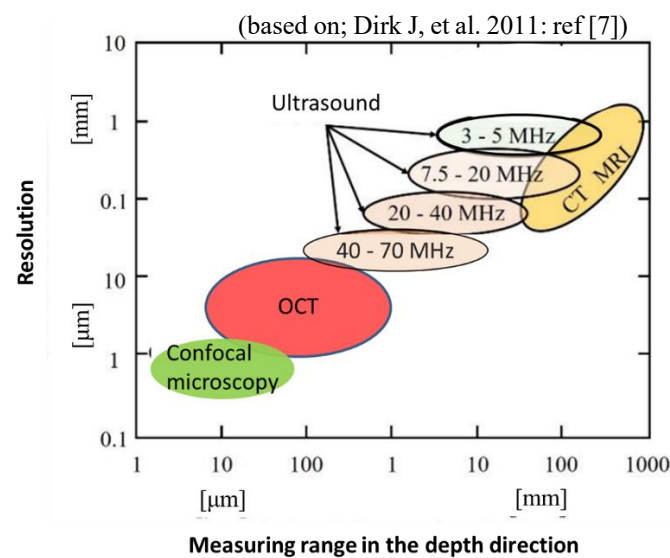


Fig. 1.1 Comparison of tomographic imaging methods.

OCT has witnessed rapid development mainly in the field of ophthalmology [11]. Through OCT measurements, the detection of diseases in the retina via photographing the cross-sectional structure of the retina is possible. Currently, it is applied for clinical diagnosis in ophthalmology and the measurement of living tissues. Figure 1.2 shows a tomographic image of a skin replica obtained through OCT measurement.

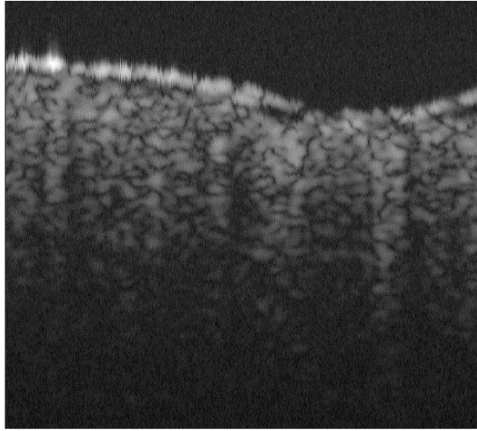


Fig. 1.2 Tomographic image of the Skin replica.

OCT uses a low-coherence light source. By spatially limiting the interference region based on the temporal coherence distance and length of this low-coherence light source, the backward scattered light at each depth position on the optical axis of the measurement sample can be measured as an interference signal [8-10]. Consequently, the spatial structure and morphology of the scatterer inside the tissue can be visualized as a tomographic image even for biological tissues, which are highly absorptive and cause considerable scattering. As mentioned above, OCT technology is now in practical use as a fundus diagnostic method in ophthalmology. Furthermore, in recent years, OCT using near-infrared light suitable for observing deeper parts of living tissues has been developed. It has the potential to spread to a wide range of fields, such as the development of endoscopic OCT [12] for diagnosis of the circulatory system and the measurement of sweat glands through skin measurement [13].

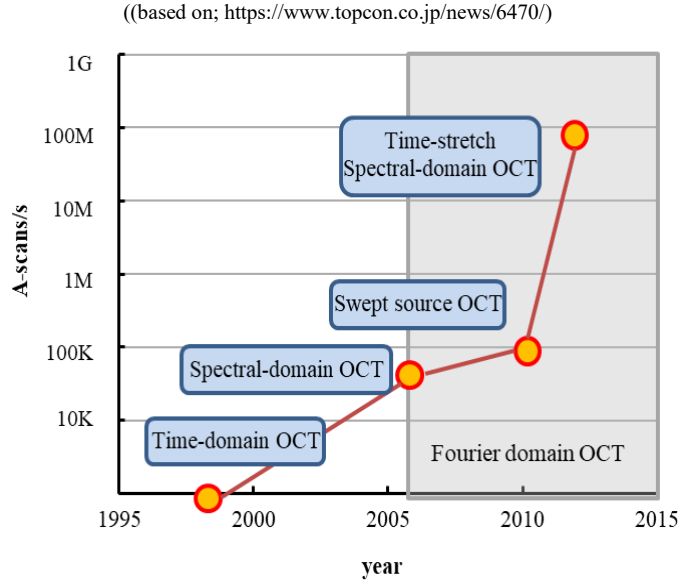


Fig. 1.3 Transition of A-scan speed of OCT.

In addition, the measurement speed of OCT has been considerably improved as shown in Fig. 1.3. The emergence of Fourier domain OCT (FD-OCT), which does not require mechanical scanning for measurements in the direction of the depth, has resulted in a considerable improvement in the measuring speed [14]. FD-OCT is a technique that measures the interference spectrum and acquires the interference signal in the depth direction via Fourier transformation. Further, spectral domain OCT (SD-OCT) [15], which measures an interference signal using a spectrometer, and swept-source OCT (SS-OCT) [16], which measures interference spectra using a wavelength-swept light source and a photodetector, are both capable of performing measurements at approximately 100 kA-scan/s. Further, as a higher-speed SD-OCT, SD-OCT using time-stretch dispersive Fourier transformation (TS-DFT) [17-21] spectroscopy is a candidate. SD-OCT uses a spectrometer that requires mechanical scanning for spectroscopy; however, TS SD-OCT can realize high-speed wavelength spectrum measurement using the TS-DFT technique

for spectroscopy. The TS-DFT-based SD-OCT using this spectroscopy enables faster measurement and achieves 100M A-scan/s [22]. The shortening of the time required for the measurement of the biological tissue using OCT is related to the reduction in the burden on the organism. Moreover, it is also being applied to biological measurements and in industrial applications such as laser welding [23]. Laser-based welding technology has been studied vigorously owing to its higher controllability than the typical plasma-based welding technology [24-25]. The laser-welding process induces three remarkable physical phenomena: a tiny hole (keyhole), which is created during the submillisecond high-power laser irradiation [26]; a metal–liquid (molten pool) phase transition [27]; and a metal–plasma phase transition [28]. Although these phenomena have been investigated by several researchers, the in-process distribution measurement of generated keyholes is yet to be demonstrated [28–33]. Optical measurement techniques are applicable to the in-process measurement of physical phenomena occurring in short periods.

Thus, OCT technology is advancing to the next stage for tomographic imaging as well as observation of morphological and structural alterations. Based on this line of thought, a full-field OCT system using a visible LED light source with the aim of evaluating dyed hair was developed [34-35]. When a living body is measured using light, it is affected by scattering and absorption that are dependent on the wavelength of light and the substances that form the living body. Scattering is a phenomenon that arises from the wave nature of light, and it propagates inside living tissues while randomly changing the propagation and deflection directions in relation to the wavelength of light, size of the scatterer, and refractive-index. The intensity of this scattering is proportional to the number density of the scatterer. In contrast, absorption is related to the wavelength of light and the molecular structure that constitutes the structure, and there exists a correlation between the intensity

of absorption and the concentration of the absorber. Therefore, information such as the number density of scatterers and the concentration of absorbers in the medium can be evaluated through measurements of the strength of these scattering and absorption phenomena. Such a measurement method is based on the Lambert-Beer law, and observation of distribution of the absorber and the scatterer of the medium was performed through the absorption and scattering measurements based on this law. The combination of OCT measurement with the Lambert-Beer law facilitates the measurement of the spatial absorption and scattering intensity of the medium. This study examined the measurement of distribution methods using OCT measurement and Lambert-Beer law with the aim of observing the water distribution and cell tissues localized inside living tissues.

In this study, we examined the dynamics of water in the tissue generated by evaporation using a method that combined OCT measurement and the Lambert-Beer law. In addition, a high-speed OCT measurement system was developed and used to examine dynamic imaging. First, it was verified that the sum of the reductions in the absorption and scattering coefficients was optimal as per the definition of the attenuation coefficient measured via OCT. The phantom was measured using a TD-OCT system utilizing 1362 nm near-infrared illumination light, and the measured value was compared with the attenuation coefficient calculated based on the Mie scattering theory. The phantom was composed of silica particles as a scatterer solidified by agar and water as an absorber. Based on the results obtained, the measurement of the attenuation coefficient was considered using a method that combined the OCT measurement and Lambert-Beer law. Consequently, the SD-OCT system was used to perform water distribution imaging and visualization of the evaporation process to observe the dynamically changing water in

tissues. Thereafter, the TS-DFT-based SD-OCT system was proposed, which enabled faster SD-OCT measurement and subsequent experimental verifications were performed. We examined a TS-DFT-base SD-OCT that operated at an A-scan rate of 10M A-scan/s was constructed and the possibility of continuous measurement.

As the first step, attenuation coefficient measurement that combined OCT measurement and Lambert-Beer law was performed, and the evaluation was performed as the absolute amount of the measured attenuation coefficient through its comparisons with the theoretical value. For the evaluation method, a phantom was prepared by mixing particles with known diameter as a scatterer, and the theoretical value of attenuation coefficient of the phantom was calculated using the Mie scattering theory. For this phantom, the attenuation coefficient measurement which combined OCT measurement and Lambert-Beer law was carried out, and it was compared with the theoretical value, and the evaluation as the absolute quantity of measured attenuation coefficient was performed. There are three types of attenuation coefficient calculation methods depending on the properties of the medium, and the attenuation coefficients calculated by each definition were verified.

As the second step, an OCT system capable of simultaneously measuring two wavelengths with different water absorption characteristics was constructed, and imaging and observation of distribution of natural evaporation were performed. Dual near-infrared illuminating lights with the wavelengths of 1060 and 1470 nm were used in the OCT. The former was not absorbed by water and the latter was absorbed by a factor of 220. Therefore, it was expected for the light scattering phenomena that only the scattering at the wavelength 1060 nm was generated by cellulose and both the scattering by cellulose and the absorption by water at 1470 nm. First, the two-wavelength OCT system was

verified through measurements of a celery stem, which has a high-water content and few scatterers. By measuring the attenuation coefficient every hour, the change in the attenuation coefficient owing to the change in the amount of water inside the sample was evaluated. Consequently, the possibility of dynamic water distribution imaging with this system was examined. Furthermore, the possibility of measuring a high-density medium such as a living body was verified. The tissue was created by compressing the leaves of dried and powdered plants. It was mainly composed of cellulose and had a refractive-index of 1.46 at near infrared wavelengths. Tissue tomographic images during the evaporation process were captured as a function of the elapsed time after the water droplets were dropped. The tomographic image of the tissue during the evaporation process and the temporal change of the attenuation coefficient were verified at two wavelengths. Subsequently, the natural evaporation was imaged and measured distribution.

The third step involved imaging and observation of distribution of the evaporation process of moist tissue under forced heating. The OCT system with single near-infrared illumination of 1470 nm was used to observe the fast variation for 30 s. The Peltier element was used as the heating system and set at 80°C. Thereafter, continuous measurement was performed at 5 s intervals to examine the possibility of real-time measurement of the evaporation process.

As the fourth step, the authors proposed a high-speed SD-OCT measurement method and developed TS SD-OCT system. The system enables dynamic acquisition of local water distribution changes in a tissue and three-dimensional image capture. It is also applicable to observation of structural alterations. This was followed by experimental

verifications. A TS SD-OCT that operated at an A-scan rate of 10M A-scan/s was constructed, and basic performance verification was conducted using a mirror as a sample.

Moreover, as a demonstration experiment, the developed system was introduced as a monitoring device of the laser welding process, and the possibility of continuous measurement was examined.

1.2 Synopsis of the Dissertation

This paper comprises 6 chapters.

Chapter 1 describes the background and purpose of the research conducted, and the structure of this paper.

In Chapter 2, the principle of OCT is described. Furthermore, the measurement principles of basic coherence laser Michelson interferometer, low coherence Michelson interferometer, TD-OCT, SD-OCT, and TS SD-OCT are described.

Chapter 3 presents the verification that the sum of the reductions in the absorption and scattering coefficients was optimal as per the definition of the absorption coefficient measured by OCT. The phantom was measured via TD-OCT system using a 1362 nm near-infrared illumination light, and the measured values were compared with the attenuation coefficient calculated using the Mie scattering theory. Consequently, the measurement of attenuation coefficient via a method that combined OCT measurement and Lambert-Beer law was examined.

Chapter 4 presents the details for constructing an OCT system that can simultaneously measure two wavelengths with different water absorption characteristics. Further, the imaging and observation of distribution of natural evaporation were verified. By measuring celery stalks with high water content and low scatterers, it was verified whether the dual-wavelength OCT system was capable of detecting water absorption. Furthermore, the possibility of measuring high-density media such as living organisms through measurements with sheet-shaped compressed leaves that were close to high-density media such as living organisms was verified.

In Chapter 5, the imaging and observation of distribution of the evaporation process of moist tissue was verified under forced heating using 1470 nm OCT. A Peltier element

was employed as a heating system and set to 80 ° C. Continuous measurement was performed to examine the possibility of real-time measurement of the evaporation process.

Chapter 6 presents the verification of the TD SD-OCT, which enabled the faster OCT measurement. The OCT measurement system that operated at approximately 10M A-scan/s was constructed, and the operation was verified. First, as a basic performance verification, an experiment using a mirror for a sample was performed, and as a demonstration experiment, it was introduced as a monitoring device of a laser welding process. Furthermore, the possibility of continuous measurement was examined.

Finally, Chapter 7 presents the conclusions of this study.

Chapter 2

Principles of Optical Coherence Tomographic Imaging

2.1 Basic concept of Optical Coherence Tomography

OCT is a tomography method that utilizes the coherence of light, and its basic structure is a measurement system that combines a Michelson interferometer with a low-coherence light source. A tomographic image that reproduces the tomographic structure of an object can be reconstructed via non-invasive, non-destructive, and non-contact measurements. Owing to its characteristics, it is applied in the medical field, particularly in the field of fundus diagnosis, as described in Chapter 1. Based on the detection of backscattered light from inside the sample as an interference signal and imaging it as a light intensity distribution at each position, a tomographic image with structural and morphological information of the measured sample can be acquired [8-10]. In addition, by using a light source with an appropriate wavelength for the medium to be measured, tomographic images with high resolution as well as non-invasive, non-contact, and non-destructive measurement can be captured. This Chapter explains the principle of the OCT method. First, the interference signal when a laser light source is used in the Michelson interferometer, which is the basis of the interferometry, is shown. In contrast, the low-coherence interferometry, upon which the TD OCT method used in this study is based, will be explained. Furthermore, the optical system of the spectral domain OCT system used in this study is shown, and the important parameters of spatial resolution and maximum measurement depth are discussed.

2.2 Laser Michelson Interferometer

The basic structure of OCT is a Michelson interferometer, which divides the emitted light from the same light source and uses optical interference to enable tomographic imaging with micron-level resolution. Figure 2.1 shows the Michelson interferometer comprising a light source, beam splitter, plane mirror, reference mirror, and photodetector. The light emitted from the light source is split by the beam splitter and radiates to the reference and the plane mirrors, respectively. The reflected light from each is recombined by the beam splitter and detected as an interference intensity signal by the photodetector.

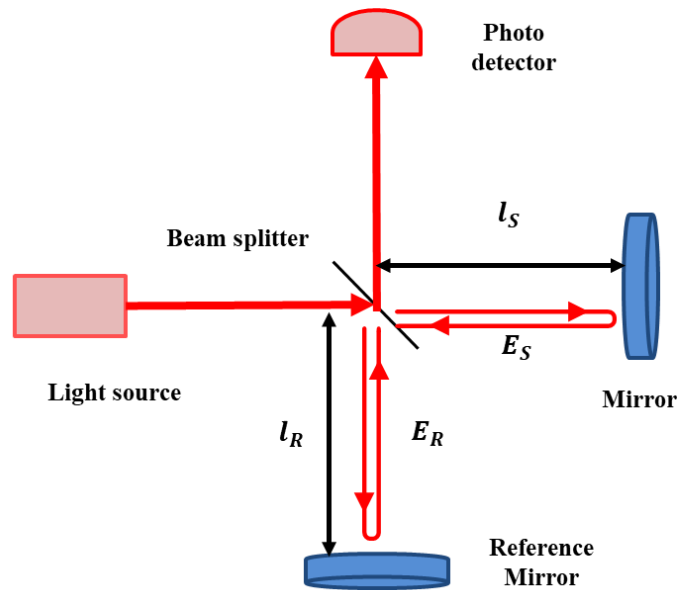


Fig. 2.1 Michelson interferometer.

E_R and E_S in Fig. 2.1 represent the reference and signal light, respectively, and l_R and l_S represent the optical path length from the beam splitter to the reference and plane mirror, respectively. Here, the light wave emitted from the light source is defined as

$$E_i(t) = E_{i0} \exp(-j\omega t) \quad (2.1)$$

Using Eq. (2.1), the reference and signal light are expressed as follows.

$$E_R(t) = E_{R0} \exp[-j(2kl_R - \omega t)] \quad (2.2)$$

	$E_S(t) = E_{S0} \exp[-j(2kl_S - \omega t)]$	(2.3)
--	--	---------

In Eq. (2.2) and (2.3), the constant 2 is because the Michelson interferometer detects the light that travels back and forth in the optical path. Here, the instantaneous intensity $I(t)$ is defined as

$$I(t) = E^*(t)E(t) \quad (2.4)$$

where $E^*(t)$ is the conjugate complex number of $E(t)$. Consider the case of actually measuring the interference light. In the visible light region, the frequency of light reaches a value as high as 10^{15} Hz, thus, a photodetector is unable to follow this. Therefore, the detected interference signal is the signal that is ensemble averaged via the response time of the photodetector. When using a light wave with stationarity and ergodicity, all ensemble averages can be replaced with time averages that are independent of the time origin. This study assumed the use of a light source with stationarity and algorithmic properties. If the above conditions are satisfied and there is a time delay Δt between the reference and signal light, setting the signal strength detected by the Michelson interferometer to $I(\Delta t)$ exhibits the following relationship

$$\begin{aligned} I(\Delta t) &= \langle I(t; \Delta t) \rangle \\ &= I_R + I_S + G_{SR}(\Delta t) \end{aligned} \quad (2.5)$$

where the time delay is related to $\Delta t = \Delta z / c$ (Δz is the optical path difference when each beam propagates), and c represents the speed of light. Further, I_R and I_S of Eq. (2.5) are the reflected light intensity of the reference and plane mirrors. The first and second terms on the right side represent the directly reflected light components. Further, the third

term is the interference light and contains information in the optical axis direction.

Focusing on this signal, there is a relationship represented by

	$G_{SR}(\Delta t) = 2\text{Re}[\langle E_S^*(t)E_R(t + \Delta t) \rangle]$ $= 2\text{Re}[\Gamma_{SR}\Delta t]$ $= 2\sqrt{I_S I_R} \gamma(\Delta t) \cos[\alpha_{SR} - \delta_{SR}(\Delta t)],$	(2.6)
--	--	-------

where $\Gamma_{SR}\Delta t$ represents the mutual coherence function, $\gamma(\Delta t)$ represents the degree of coherence, α_{SR} represents the constant phase, and $\delta_{SR}(\Delta t)$ represents the phase lag.

The mutual coherence function is a cross-correlation function of reference and signal light, and the phase lag $\delta_{SR}(\Delta t)$ is expressed as $\delta_{SR}(\Delta t) = 2\pi\nu_0 \Delta t = \omega \Delta t$. The interfering light observed in case of Eq. (2.6) changes owing to time delay or optical path difference.

Subsequently, using the Wiener–Khinchin theorem [13], the power spectrum of the light source $S_{sources}(\nu)$ is expressed as the Fourier transform of the coherence function $S_{sources}(\tau)$ of the light source expressed as

$$S_{sources}(\nu) = \text{FT}[\Gamma(\Delta t)], \quad (2.7)$$

where FT represents the Fourier transform, the coherence function of the light source is the autocorrelation function of the light source. Further, $W_{SR}(\nu)$ is the mutual spectral density of the reference and signal light, and is obtained via the Fourier transform of the mutual coherence function $\Gamma_{SR}(\Delta t)$ as

$$W_{SR}(\nu) = \text{FT}[\Gamma_{SR}(\Delta t)] \quad (2.8)$$

Then, using the time delay Δt , the spectral interference is expressed as

$$S(\nu; \Delta t) = S_S(\nu) + S_R(\nu) + 2\text{Re}[W_{SR}(\nu)] \cos(2\pi\nu\Delta t) \quad (2.9)$$

Here, as shown in Fig. 2.1, the interferogram acquired by the photodetector when the reference and plane mirrors are arranged is expressed as

$$\begin{aligned}
G_{SR}(\tau) &= 2\text{Re}[\Gamma_{SR}(\tau)] \\
&= 2\text{Re}[\Gamma_{source}(\tau)] \\
&= G_{source}(\tau)
\end{aligned} \tag{2.10}$$

The interferogram between the mirrors is obtained from twice the real part of the mutual coherence function, as shown in Eq. (2.10). In addition, owing to the mirrors being arranged, the interferogram can be calculated considering twice the real number of the coherence function of the light source, and the signal at this time is defined as G_{source} . Further, the interferogram when a sample with a backscatter profile of $h(\tau)$ is placed on the plane mirror side is expressed as

$$\begin{aligned}
G_{SR}(\tau) &= 2\text{Re}[\Gamma_{SR}(\tau)] \\
&= 2\text{Re}[\Gamma_{source}(\tau) * h(\tau)]
\end{aligned} \tag{2.11}$$

The interferogram detected by the photodetector using Eq. (2.11) is the real part of the convolution of the backscattering profile of the sample and coherence function. Moreover, if Eq. (2.11) is expressed as an interferogram in the frequency domain, it is expressed as

$$W_{SR}(\nu) = S_{source}(\nu)H(\nu), \tag{2.12}$$

where $H(\nu)$ represents the sample transfer function, and there exists a relation as $H(\nu) = \text{FT}[h(t)]$. Using the relational expression shown above, a comparison of the interference waveforms using the high- and low-coherence light in the Michelson interferometer composed of the reference and plane mirrors is shown in Fig. 2.1.

First, consider the case where ideal laser light, that is, high-coherence light, is used as the light source. In the case of an ideal laser light source, only a specific wavelength is output expressed as

$$S_{source}(\nu) \propto \delta(\nu - \nu_0) \tag{2.13}$$

In this case, the interferogram obtained by the photodetector is expressed as

$$G_{\text{Source}}(z) \propto 2\text{Re}[\Gamma_{\text{Source}}(z)]$$

$$\propto \cos\left(\omega_0 \frac{z}{c}\right) \quad (2.14)$$

In Eq. (2.10), it is expressed as a relational expression of a time variable; however, in Eq. (2.14), it is expressed via a relational expression with an optical path difference as a variable. of the relationship in Eq. (2.14) shows that the interferogram acquired using a high-coherence laser light source fluctuates sinusically with the optical path difference between the reference and plane mirrors as a variable. Based on the above results, Figs. 2.2 (a) and (b) show the spectrum diagram of the light source and the detected interferogram.

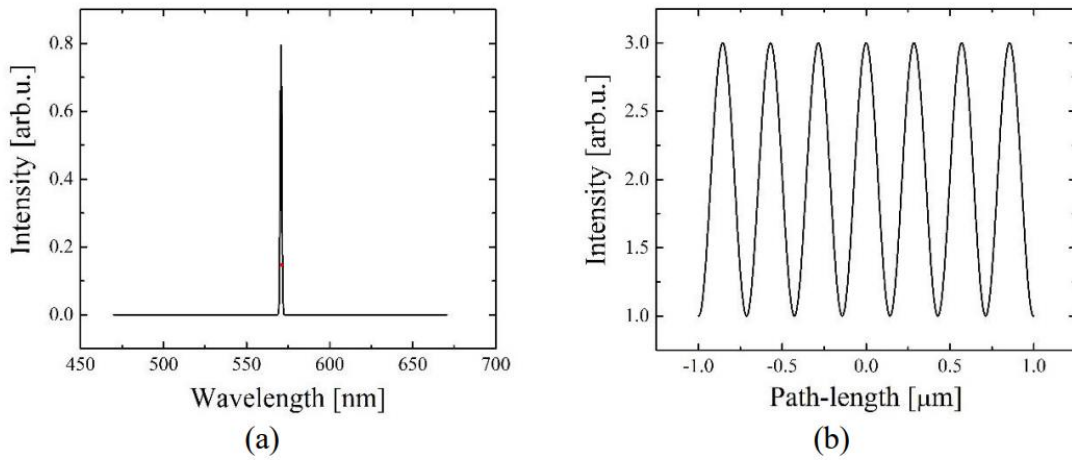


Fig. 2.2 (a) High-coherence laser spectrum, (b) Interferogram using high-coherence laser source.

From Fig. 2.2 (b), when a high-coherence laser beam is used as the light source, a periodic interferogram is formed owing to the optical path difference. Therefore, the positional relationship between the reference and plane mirrors cannot be satisfied. Next, consider

the case where low-coherence light such as Super Luminescent Diode (SLD) or LED is used as the light source of the Michelson interferometer. For low-coherence light sources, the power spectrum of the light source can be approximated to a Gaussian distribution, which is expressed as

$$S_{\text{Source}}(\nu) \propto \exp \left\{ -4 \log 2 \left(\frac{\nu - \nu_0}{\Delta \nu} \right)^2 \right\}, \quad (2.15)$$

where \log represents the natural logarithm. When using a light source such as Eq. (2.15), the detected interferogram is expressed as

$$\begin{aligned} G_{\text{Source}}(z) &= 2\text{Re}\{I_{\text{Source}}(z)\} \\ &\propto \exp \left\{ -4 \ln 2 \left(\frac{z}{l_{\text{FWHM}}} \right)^2 \right\} \cos \left(\frac{2\pi}{\lambda_0} z \right) \\ &= \exp \left\{ - \left(\frac{\pi \Delta \nu z}{2c\sqrt{\ln 2}} \right)^2 \right\} \cos \left(2\pi \nu_0 \frac{z}{c} \right) \end{aligned} \quad (2.16)$$

In general, the Fourier transform of a Gaussian function is another Gaussian function, thus, as shown in Eq. (2.16), the obtained interferogram also exhibits a Gaussian distribution. The coherence length l_c is expressed as

$$\begin{aligned} l_c &= \frac{l_{\text{FWHM}}}{2} \\ &= \frac{2 \log 2}{\pi} \frac{\lambda_0^2}{\Delta \lambda}, \end{aligned} \quad (2.17)$$

where $\Delta \lambda$ is the spectral width and λ_0 is center wavelength of the light source. In Eq. (2.17), l_{FWHM} (Full Width at Half Maximum of Gaussian distribution) is divided by 2, because the Michelson interferometer incorporates the fact that it detects the

reciprocating light. Based on the above results, Figs. 2.3 (a) and (b) show the spectrum diagram of the light source and the detected interferogram.

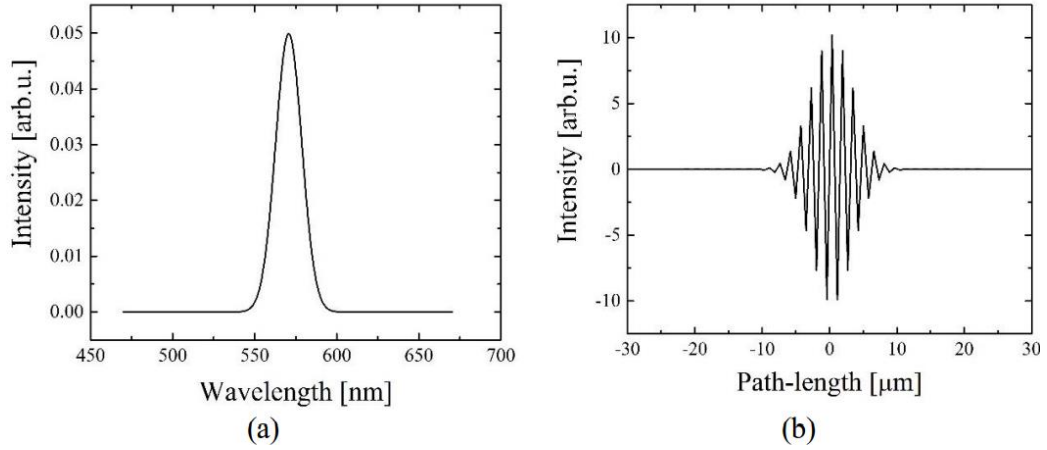


Fig. 2.3 (a) Low-coherence laser spectrum, (b) Interferogram using Low-coherence laser source.

From Fig. 2.3 (b), when low-coherence light such as LED or SLD is used, the Gaussian distribution is localized in the interferogram acquired at the point where there is almost no optical path difference. Based on this relationship, the positional relationship between the reference and planar mirror can be determined in the Michelson interferometer using a low-coherence light source. The OCT, which uses a Michelson interferometer employing a low-coherence light source, selectively detects the position of the reflection point inside the sample, thus rendering the capture of tomographic images without contacting the sample possible.

2.3 Time-Domain OCT (TD-OCT)

The TD-OCT devised based on the Michelson interferometer specified in Section 2.2 is explained [36]. First, Fig. 2.4 shows the method for acquiring information on the TD-OCT optical system and the inside of the measurement sample.

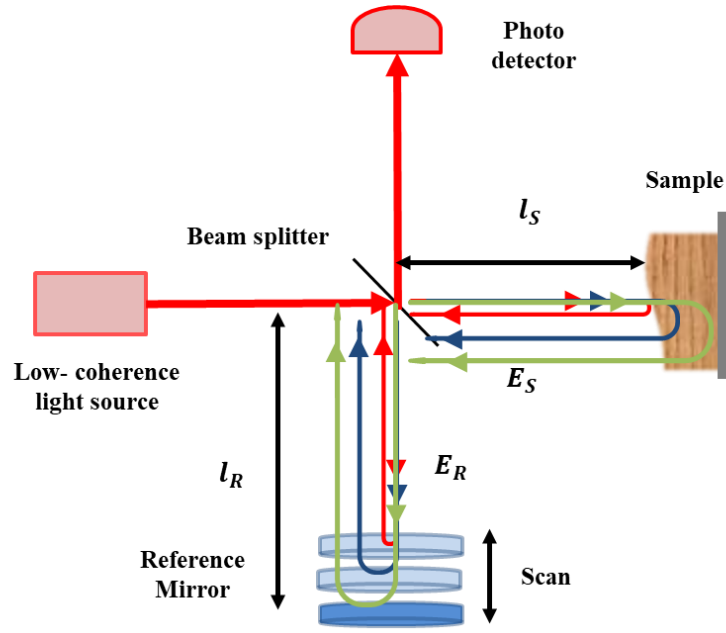


Fig. 2.4 Time-domain OCT.

The TD-OCT is a Michelson interferometer system that uses a low-coherence light source; however, the main change is that the plane and reference mirror sides can be used as the measurement sample and scanned in the optical axis direction, respectively. In Fig. 2.4, the structure is such that the reference mirror side is scanned; however, the same result can be obtained by scanning the sample side in the optical axis direction. In TD-OCT, based on performing mechanical scanning in the optical axis direction, localized interference light intensity is detected at points where the optical path differences are approximately identical. In addition, tomographic imaging at the irradiation point is

rendered possible by obtaining information at each reflection point of the layered sample. Acquiring the information inside this measurement sample is referred to as A scan. The optical axis resolution Δz by OCT is expressed as

$$\begin{aligned}\Delta z &= l_c \\ &= \frac{2 \log 2}{\pi} \frac{\lambda_0^2}{\Delta \lambda},\end{aligned}\tag{2.18}$$

where the optical axis resolution Δz is equal to the coherence length l_c of the light source, thus, it can be calculated from Eq. (2.17). Based on this relationship, the optical axis resolution is determined by the center wavelength and wavelength bandwidth of the light source used, and its value ranges from several μm to several tens of μm . With TD-OCT, point detection is performed via focusing and irradiating the measurement sample, and two- or three-dimensional tomographic images can be captured by scanning the optical axis in the direction perpendicular to the optical axis. Moreover, based on this TD-OCT, Full-Field OCT (FF-OCT) can be constructed, which eliminates the need for scanning in the vertical direction of the optical axis by irradiating the measurement sample with parallel light and detecting it using a two-dimensional detector. Finally, regarding the measurement time, as the TD-OCT requires a mechanical scan to perform the A scan, a longer measurement time is required than the FD-OCT described in the next section.

2.4 Spectral-Domain OCT (SD-OCT)

SD-OCT is a method that can acquire information in the depth direction of a measurement sample through the detection of an interference signal in the wavelength spectrum and performing an inverse Fourier transform. In contrast to TD-OCT, information in the sample depth direction can be acquired without mechanical scanning, which results in faster tomographic imaging than TD-OCT [16]. In addition, in contrast to TD-OCT, SD-OCT treats interference signals generated from all depths as image information, thus, it exhibits a measurement sensitivity approximately 30 times higher than that of TD-OCT. The SD-OCT system is shown in Fig. 2.5.

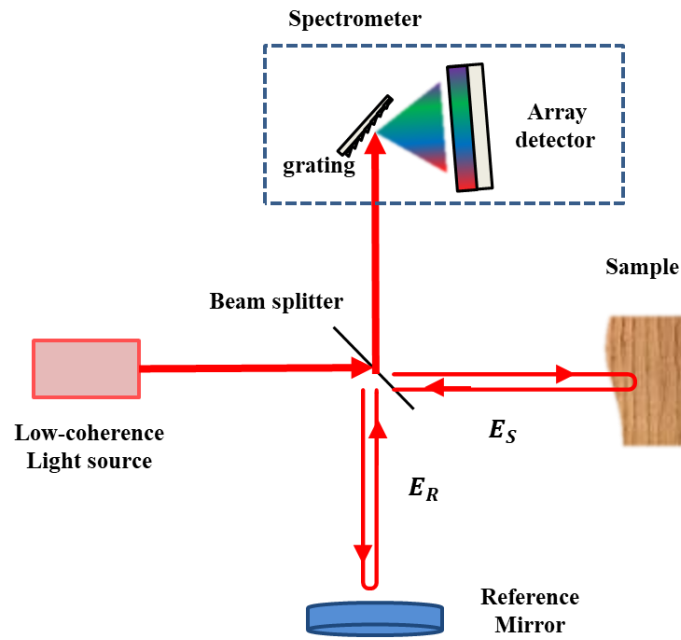


Fig. 2.5 Spectral-domain OCT.

The interference spectra obtained on the spectroscopy is the intensity $I(k)$ on the wavenumber axis, and is expressed as

$$I(k) \propto S(k) \int_0^\infty a(z) \cos(2knz) dz, \quad (2.19)$$

where $S(k)$ is the spectra intensity distribution of the light source, k is the wavenumber, z is the depth of the measured sample, $a(z)$ is the backscattered light amplitude at the depth z , and n is the refractive-index of the sample. The depth direction signal intensity distribution $I(z)$ is obtained via the Fourier transform of the interference light spectrum $I(k)$ acquired by the spectroscopy, and is expressed by the time required for the optical path as follows

$$I(z) \propto FT^{-1}[I(k)]. \quad (2.20)$$

Each reflection point information in the measurement sample is expressed by the time required for the optical path and corresponds to the distance. Figure 2.6(a) shows the interferogram acquired by the spectroscopy when the light source exhibited an ideal Gaussian distribution and there was a slight optical path difference between the reference mirror and the sample surface. Figure 2.6(b) shows the result of the inverse Fourier transform of the interferogram.

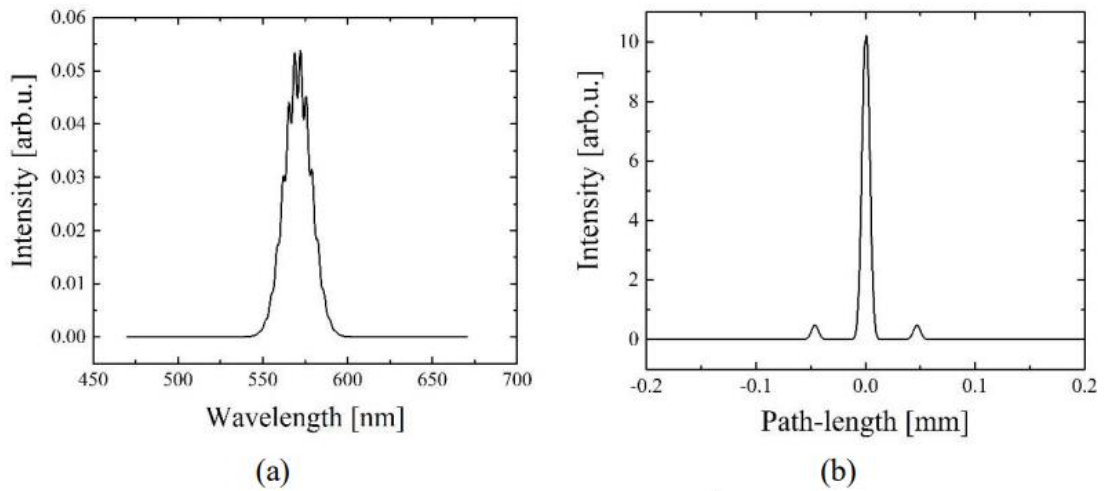


Fig. 2.6 (a) Interferogram, (b) inverse Fourier transform of the interferogram.

Figure 2.6 (a) shows the interference signal intensity distribution acquired on the spectroscope. Figure 2.6 (b) shows the signal intensity distribution obtained by performing inverse Fourier transform on the interference signal intensity distribution, extracting the real part of the converted signal, and performing square processing. Here, in the actual spectroscopic detection, as it was detected as a discrete signal, FFT was performed to acquire the depth direction information of the sample. As shown in Fig. 2.6(b), as the Fourier transform of the real signal cannot distinguish between the frequencies in the positive and negative regions, signals of the same intensity appeared in both the positive and negative optical path differences. Herein, the optical path difference was 0 at the center. In addition, when the optical path difference was approximately 0, the signal implied the DC component. In the actual OCT tomographic image, the negative area was not displayed, and the positive area was extracted as the tomographic image. Thus, only the positive part was treated in the signal intensity distribution of SD-OCT. Next, in contrast to the TD-OCT, the principle that A scan is possible without performing mechanical scan is explained. As shown in Eq. (2.20), the interference light is a periodic component of a sine wave with respect to the optical path difference. For a small optical path difference, the frequency of the interference signal becomes small owing to the period in the sine wave being small. Therefore, a coarse waveform was detected by the spectroscope. A small optical path difference implies measurement of a shallow part of the sample. However, when the optical path difference is large, the frequency of the interference signal increases owing to the period in the sine wave being large. Therefore, a fine waveform was detected by the spectroscope. A large optical path difference implies measurement of the deep part of the sample. Here, assuming the case where signals of two frequencies are detected, the signal intensity distribution shown in Fig. 2.7 (a) was

multiplied by the high-frequency sinusoidal component. Figure 2.7 shows the interferogram at that time and the result of converting the signal into a signal intensity distribution with the optical path length difference as a variable via the inverse Fourier transform of the signal.

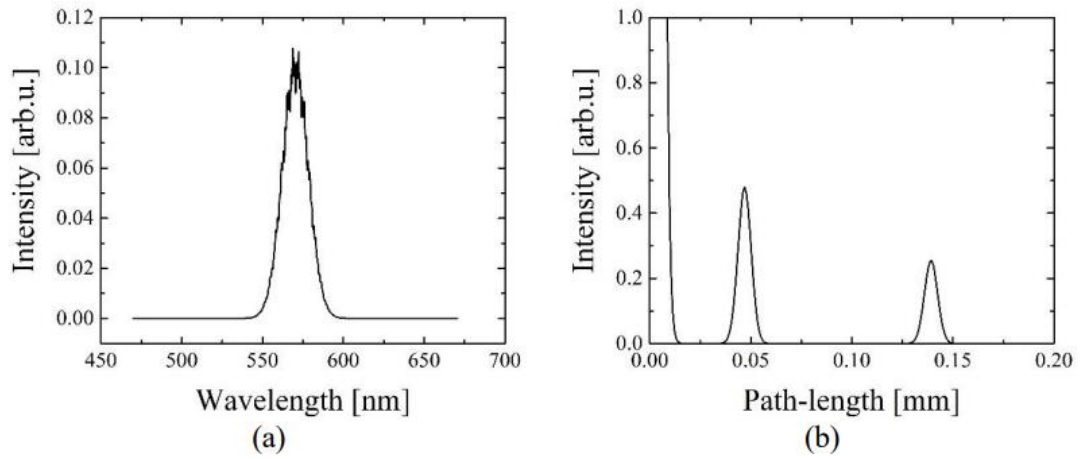


Fig. 2.7 (a) Interferogram, (b) inverse Fourier transform of the interferogram.

In Fig. 2.7 (b), the scale was set in the range of 0 –0.2 mm on the horizontal axis and 0–1.0 on the vertical axis. Two different frequency components were detected separately via the inverse Fourier transform. In SD-OCT, interference signals with multiple frequency components generated from reflected light from multiple depth in the sample were superimposed and detected; however, they can be detected separately by the inverse Fourier transform. In this way, SD-OCT renders it possible to acquire the signal distribution in the depth direction with a single shot. Based on the above principle, the sample depth direction information can be acquired faster than TD-OCT. In SD-OCT, the measurable range z_{max} in the optical axis direction is determined by the followability to the period of the sine wave. z_{max} is expressed as

$$z_{max} = \frac{1}{4n_{ave}} \frac{\lambda_0^2}{\delta\lambda} , \quad (2.21)$$

where n_{ave} is the average refractive-index inside the measurement sample, λ_0 is the center wavelength of the light source, and $\delta\lambda$ wavelength resolution of the spectroscopy. The coefficient 1/4 on the right side is generated because the number of data is halved by FFT and the Michelson interferometer detected the round-trip optical path. As the followability of this sine wave is determined based on the wavelength resolution of the spectroscopy, the measurement range in the depth direction is determined by the performance of the spectroscopy in SD-OCT. The depth direction resolution in SD-OCT is determined by the center wavelength and wavelength bandwidth of the light source as shown in Eq. (2.18), similar to that in TD-OCT.

2.5 Time-Stretch SD-OCT (TS SD-OCT)

Similar to the case of SD-OCT, TS SD-OCT can detect the interference signal of the wavelength spectrum and obtain the information of the depth direction of the measurement sample by performing Fourier inverse transforms. SD-OCT uses a spectrometer that requires mechanical scanning for spectroscopy; however, TS SD-OCT can realize high-speed wavelength spectrum measurement using the time-stretch dispersion Fourier transform (TS DFT) technique for spectroscopy [20-21]. TS-DFT converts a short pulse into a chirp pulse through the propagation of an ultrashort pulse light in a high dispersion medium such as an optical fiber, detects the chirp pulse waveform by a high-speed photodetector and a real-time oscilloscope, and measures the spectrum of each pulse.

The measurement speed of this method is equal to the repetition frequency of ultrashort pulse light, and thus spectroscopic measurements can be conducted from several tens MHz to GHz. The TS SD-OCT system is shown in Fig. 2.8.

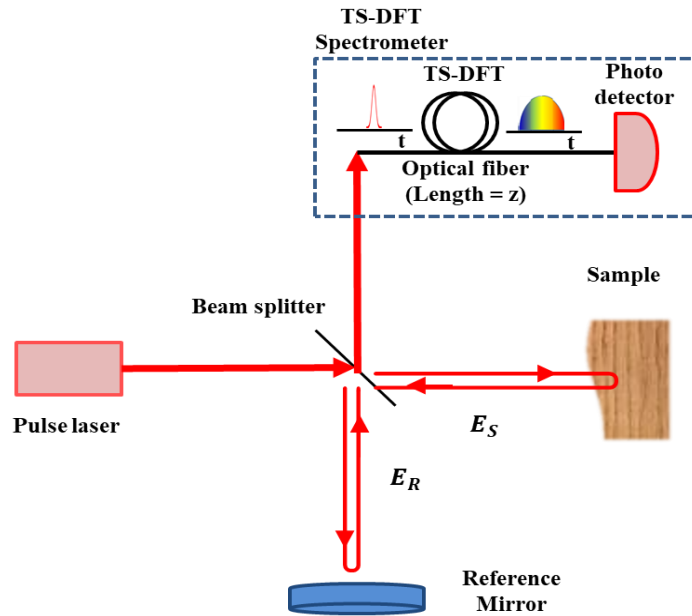


Fig. 2.8 TS SD-OCT

In the TS-DFT section, the ultrashort pulse is temporally extended by the influence of the wavelength dispersion while propagating in the optical fiber, and is transformed into a chirp pulse. The dispersion coefficient of an optical fiber can be expressed as

$$\beta = \beta_0 + \beta_1\Omega + \frac{1}{2}\beta_2\Omega^2 + \dots, \quad (2.22)$$

where $\Omega = \omega - \omega_0$. where ω_0 is the central angular frequency, β_0 is the group refractive-index, β_1 is the group delay, and β_2 is the group velocity dispersion [28].

The electric field after propagation over distance z in the optical fiber is expressed as

$$E(z, t) = \frac{1}{2\pi} \int_{-\infty}^{+\infty} \tilde{E}(0, \omega) \exp [i(\omega t - \beta z)] d\omega, \quad (2.23)$$

where $\tilde{E}(0, \omega)$ represents the spectrum of the incident ultrashort pulse. For a sufficiently large dispersion, the electric field of the light is approximated as

$$E(z, t) = \frac{1}{2\pi} \tilde{E}(0, \frac{T}{\beta_2 z}) \exp \left[i(\omega_0 T + \frac{T^2}{2\beta_2 z}) \right], \quad (2.24)$$

The ultrashort pulse is changed to a chirped pulse with a chirp rate of $1 / \beta_2 z$, where T is the shifted time caused by the propagation in the optical fiber, $T = t - \beta_1 z$. Using Eq. (2.24), as the time waveform of the optical electric field after long-distance fiber propagation is similar to the spectrum of light, the power spectral of one original ultrashort pulse can be measured by measuring the time waveform of the light intensity.

Next, the interference of time-stretched light is explained. The electric fields of the reference light, E_r , and the signal light, E_s , at the optical detector are, respectively expressed as

$$E_r(t) = E_{r0} \exp \left[i(\omega_0 T_r + \frac{T_r^2}{2\beta_2 z}) \right] \tilde{E}(0, \frac{T_r}{\beta_2 z}) \quad (2.25)$$

and

$$E_s(t) = E_{s0} \exp \left[i(\omega_0 T_s + \frac{T_s^2}{2\beta_2 z}) \right] \tilde{E}(0, \frac{T_s}{\beta_2 z}), \quad (2.26)$$

where T_r is the time of reference light, and T_s is the time of signal light, the relationship between T_r and T_s is $T_s = T_r - \Delta l / c$. Here, Δl is the difference between the reference and signal light path lengths, and c represents the speed of light. Further, E_{r0}

is the amplitude of the reference light, and E_{s0} represents the amplitude of the signal light. These light components interfere in the detector, and the intensity, I , is expressed as

$$\begin{aligned}
I(t) &= [E_r(t) + E_s(t)][E_r(t) + E_s(t)]^* \\
&= (E_{r0}^2 + E_{s0}^2)S(T_r) \\
&\quad + 2E_{r0}E_{s0}S(T_r)R_e \left\{ \exp \left[i \left(\frac{\Delta l}{c\beta_2 z} T_r - \frac{\Delta l^2}{2c^2\beta_2 z} T_r + \omega_0 \frac{\Delta l}{c} \right) \right] \right\},
\end{aligned} \tag{2.27}$$

where $S(T_r)$ is assumed as follows because the time difference between the reference and signal light is extremely smaller than the pulse width.

$$\begin{aligned}
S(T_r) &= \left| \tilde{E} \left(0, \frac{T_r}{\beta_2 z} \right) \right|^2 \\
&\cong \left| \tilde{E} \left(0, \frac{T_s}{\beta_2 z} \right) \right|^2 \\
&\cong \tilde{E} \left(0, \frac{T_r}{\beta_2 z} \right) \tilde{E}^* \left(0, \frac{T_s}{\beta_2 z} \right) \\
&\cong \tilde{E}^* \left(0, \frac{T_r}{\beta_2 z} \right) \tilde{E} \left(0, \frac{T_s}{\beta_2 z} \right)
\end{aligned} \tag{2.28}$$

The interference signal oscillates sinusoidally in time. The beat frequency is $\Delta l / \beta_2 z$, which is proportional to the path length (Δl), and the chirp rate of the optical fiber is $1/\beta_2 z$.

The relationship between the approximated and measured length $|\Delta l|$ is calculated based on the third part of Eq. 6 as follows:

$$|\Delta l| = 2\pi f c \beta_2 l_0 = |-f \lambda^2 D l_0|, \tag{2.29}$$

where f represents the peak frequency of the interference spectrum, D [ps/nm/km] denotes the dispersion coefficient of DCF, and l_0 [km] represents the length of the fiber.

Next, consider the measurement characteristics in TS SD-OCT. The measurement range in the depth direction is expressed as Eq. (2.20) similar to that of SD-OCT. The resolution in the depth direction is inversely proportional to the wavelength resolution of the

spectrometer, and the wavelength resolution of the time-stretch spectroscopy is expressed as $\delta_\lambda = \delta_t/D$, where δ_t is the temporal resolution of the detection system and D is the total group velocity dispersion (GVD) of the dispersive fiber. The measurement resolution in the depth direction is determined by the center wavelength and wavelength bandwidth of the light source as shown in Eq. (2.18), as in SD-OCT.

2.6 Conclusions

This Chapter explained the Michelson interferometer using a laser light source, which is the basis of the interference method, and showed the interference signal detected by the high coherence Michelson interferometer. In contrast, the low coherence Michelson interferometer, which is the basic structure of OCT, was explained and the interference signal was shown. Subsequently, the principle of TD-OCT based on the low coherence Michelson interferometer was described, and the basic optical system and performance in measurement were explained. Further, the principle of SD-OCT based on the low coherence Michelson interferometer was described, compared with TD-OCT, and the basic optical system and performance in measurement were explained. Finally, the principle of TS DFT based SD-OCT, which enables the speedup of SD-OCT was described, and the basic optical system and performance in the measurement were explained.

Chapter 3

Evaluation of Attenuation Coefficient using Optical Coherence Tomography

3.1 Introduction

We have focused on the spectroscopic measurement and imaging of the attenuation coefficient owing to scattering and absorption as an application of OCT to biopsy. The attenuation coefficient expresses the degree of decreasing light intensity when light incident on the medium propagates under scattering and absorption, which is defined by the Beer-Lambert law. An example of quantitative measurement of attenuation coefficients for biological tissues is a pulse oximeter [38]. The blood oxygen saturation is estimated by the ratio of absorption at red light to that at near-infrared light, which exhibits different absorption characteristics of hemoglobin. Schmitt et al. [39] and Thrane et al. [40] proposed an extended Huygens-Fresnel (EHF) model that considers the effect of multiple scattering on the single-scattered light in the quasi-retroreflection direction. The EHF model has been experimentally verified and confirmed to be a useful theoretical model [41,42]. However, the theoretical equation based on the EHF model is plagued by certain difficulties when used as a measurement method. There are two unknown variables, the scattering coefficient and the effective beam size inside the medium under the influence of multiple scattering, which require the use of transmission-type OCT and a wide range for fitting the model function to the intensity variation.

This Chapter presents a description of the measurement of the absolute value of the attenuation coefficient via the direct application of the Beer-Lambert law to the intensity

variation in the depth direction (A-scan) obtained by OCT measurement. There are three definitions of the attenuation coefficient: the sum of the scattering and absorption coefficients, the sum of the reduced scattering and absorption coefficients, and the effective attenuation coefficient that is an analytical solution of the one-dimensional photon diffusion equation. Empirical experiments were conducted to determine the definition best suited for application to the A-scan intensity variation obtained by OCT measurement. A phantom composed of silica-particle suspension solidified by agar was used in the experiment. The sum of the reduced scattering and the absorption coefficients was determined to be the best definition as the attenuation coefficient for the A-scan intensity variation. Consequently, the cross-sectional image of the local attenuation coefficient was reconstructed via the successive application of the Beer-Lambert law to a finite range of the A-scan position in the cross-sectional image of the OCT intensity. Furthermore, the cross-sectional image of local silica-particle concentration was reconstructed using the cross-sectional image of the local attenuation coefficient and the Mie scattering theory. Thus, we succeeded in clearly observing the fibrous structure generated by agar solidification via the scattering phenomenon from the silica particles accumulated in it.

3.2 Definitions of Attenuation Coefficient in OCT measurement

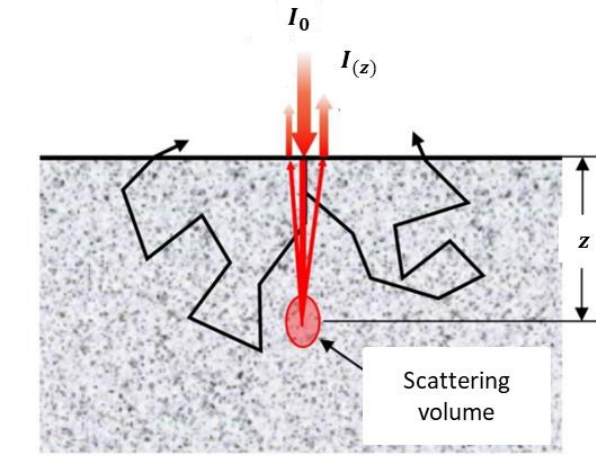


Fig. 3.1 Quasi-rectilinearly propagation of light scattered from the scattering volume at the depth z , which is limited by the temporal coherence length of the light source and the beam size of the illuminating light.

Figure 3.1 shows the principle used for the analysis of attenuation coefficients using OCT. The scattering volume at the depth z is limited by the illuminating beam size inside the medium and the temporal coherence of the light source. The OCT intensity is detected when the quasi-rectilinearly propagated light scattered from the scattering volume interferes with the reference light. Therefore, as evident, OCT can detect selectively single-scattered light propagating quasi-rectilinearly in the both ways between the surface and the scattering volume [40,41]. For such a phenomenon, the Beer-Lambert law is expressed as

$$I(z) = I_0 \exp(-2\mu_t z) \quad (3.1)$$

This is applied to estimate the attenuation coefficient of the medium. The coefficient 2 in Eq. (3.1) implies that the light propagates back and forth between the surface and the depth z . There are three definitions of the attenuation coefficient, depending on the state of the medium:

$$\mu_t = \begin{cases} \mu_s + \mu_a & (3.2a) \\ \mu'_s + \mu_a & (3.2b) \\ \sqrt{3\mu_a(\mu'_s + \mu_a)} (= \mu_{\text{eff}}) & (3.2c) \end{cases}$$

where μ_t is the attenuation coefficient, μ_s the scattering coefficient, μ'_s the reduced scattering coefficient, and μ_a the absorption coefficient.

Equation (3.2a) is the attenuation coefficient defined for dilute solution. The light scattered from the particles dispersed independently directly reach the detector and are detected as an incoherent sum of scattering intensities. The attenuation coefficient is obtained via the product of the attenuation cross section of a single scatterer and the number density of the scatterer, and is expressed as

$$\mu_t = n\sigma_t = n(\sigma_s + \sigma_a) \quad (3.3)$$

where σ_t is the attenuation cross section, σ_s the scattering cross section, σ_a the absorption cross section, and n is the number density of scatterers.

Further, μ'_s in Eq. (3.2b) is the reduced scattering coefficient, which is defined using the scattering coefficient μ_s as follows:

$$\mu'_s = (1 - g)\mu_s \quad (3.4)$$

where g is the anisotropic scattering coefficient or the g -parameter. It is defined as the average of the cosine of the scattering angle over all solid angles:

$$g = \langle \cos\theta \rangle = \int_{4\pi} p(\Omega) \cos\theta \, d\Omega \quad (3.5)$$

where $p(\Omega)$ is the phase function of the scattering. The g -parameter increases consistently with increased in the size of the scatterer up to 1. This is because the anisotropy of the scattering field increases consistently with the forward scattering component that propagates in the direction of the incident light. With decrease in the size of the scatterer, the g -parameter converges to 0, at which point the scattering becomes isotropic. As expressed in Eq. (3.4), $(1 - g)$ multiplied by the scattering coefficient

represents the sum of non-forward scattering components. Therefore, the reduced scattering coefficient includes the influence of low-order multiple scattering.

The attenuation coefficient in Eq. (3.2c) is the analytical solution of the one-dimensional photon diffusion equation for the multiple-scattering field, that is, a diffusion field of light energy generated by a point diffuse source. The diffusion intensity at the distance z from the point diffuse source is analytically obtained as

$$I(z) = \frac{\mu_{\text{eff}}}{2\pi} e^{-\mu_{\text{eff}}z} \quad (3.6)$$

The coefficient of the exponential part is referred to as the effective attenuation coefficient and expressed as

$$\mu_{\text{eff}} = \sqrt{3\mu_a(\mu'_s + \mu_a)} \quad (3.7)$$

This study experimentally determined the best definition in the attenuation coefficients shown in Eq. (3.2).

3.3 Experimental Systems and Procedures

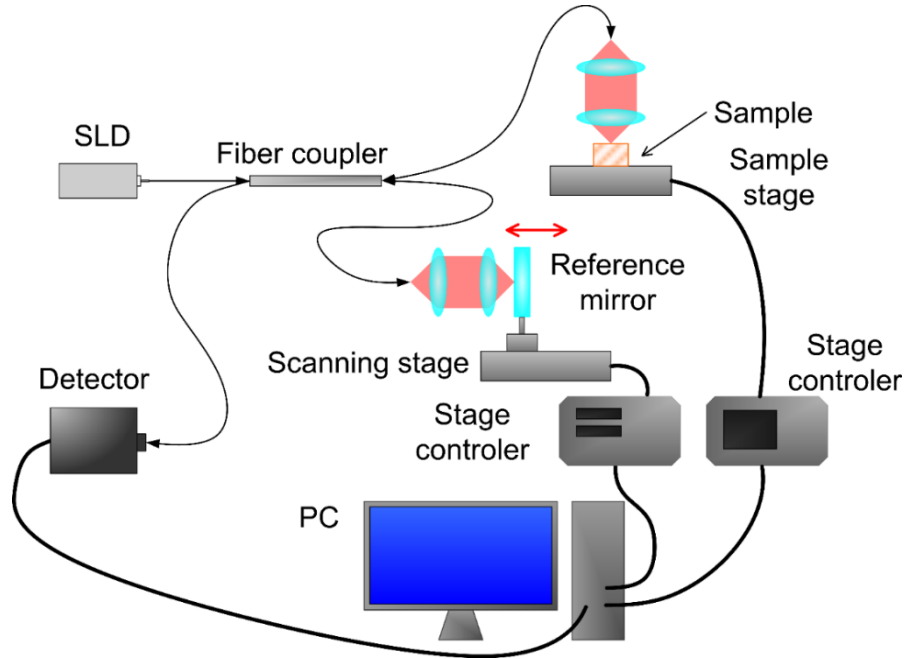


Fig. 3.2 Fiber-optic OCT system in the time domain.

Figure 3.2 shows the fiber-optic OCT system in the time domain. The light emitted from the SLD was guided by a single-mode fiber and split into two light waves using a fiber coupler (Thorlabs, TW1300R5A2) with a split ratio of 1:1 toward a sample and a reference mirror. The split light waves were collimated by collimating lenses and focused onto the sample and the reference mirror using an objective lens (Olympus, MPLanFLN 5X). The backscattered and reflected light generated from the sample and reference mirror, respectively, were recombined using the fiber coupler and detected via a detector as the interference intensity. Subsequently, the interference intensity signal was quantized to a 12-bits digitized signal using an A/D conversion board, transferred to a computer as digital data, and reconstructed into the cross-sectional image.

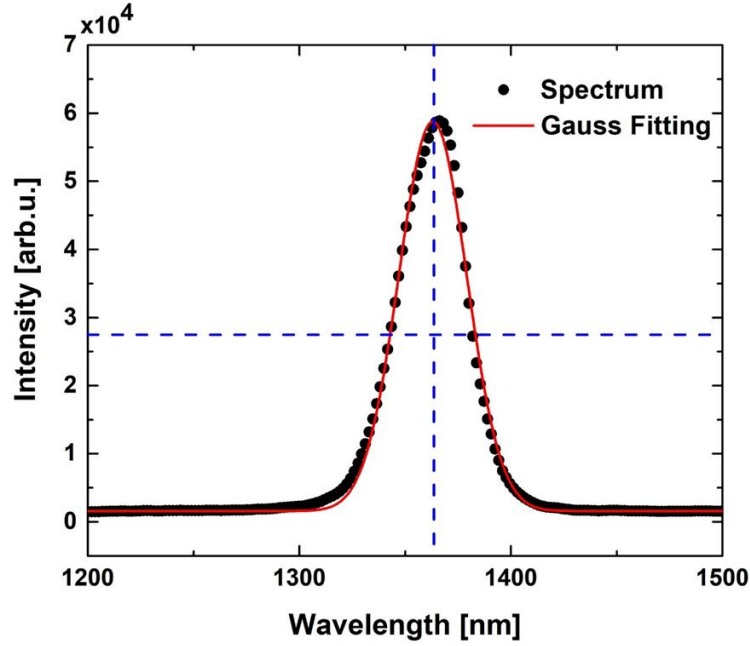


Fig. 3.3 Emission spectrum of a near-infrared SLD with the central wavelength of $\lambda_0=1362$ nm and the bandwidth of $\Delta\lambda=38$ nm.

The intensity spectrum of the SLD (Thorlab, SLD1325) is shown in Fig. 3.3, whose central wavelength and bandwidth were $\lambda_0=1362$ nm and $\Delta\lambda=38$ nm, respectively. The A-scan resolution is equal to the temporal coherence length of the SLD, which is expressed as

$$l_c = \frac{2 \ln 2}{\pi} \cdot \frac{\lambda_0^2}{\Delta\lambda} \quad (3.8)$$

Using Eq.(3.8), the resolution of the A-scan was $l_c=22$ μm . The resolution of the lateral scan corresponded to the focused beam size, which had diameter of 5.8 μm . The A-scan was performed by moving the reference mirror, whose maximum depth was 752 μm . As the reference mirror is scanned at a constant speed in the TD-OCT, the time-varying interference signal is measured via heterodyne detection at the Doppler shift frequency.

Further, the lateral scanning was performed employing a stepping-motor-driven stage and the sample was A-scanned at 20 points over a distance of 100 μm .



Fig. 3.4 Phantom of the silica particle suspension solidified by agar.

Figure 3.4 shows the phantom of the silica-particle suspension solidified by agar. The phantom was turned upside down in the experiment because the particles settled down during the agar solidification. The silica particle as a scatterer exhibited no absorption in the visible to near-infrared regions, and had a refractive-index and particle radius of 1.46 and 0.25 μm , respectively. Water was employed as the absorber of the phantom, with an absorption coefficient of 4 cm^{-1} at 1362 nm as per the absorption spectrum shown in Fig. 3.5. In the experiment, six types of the phantoms with volume concentrations of 0.5, 1, 2, 3, 4, and 5 vol.% were prepared.

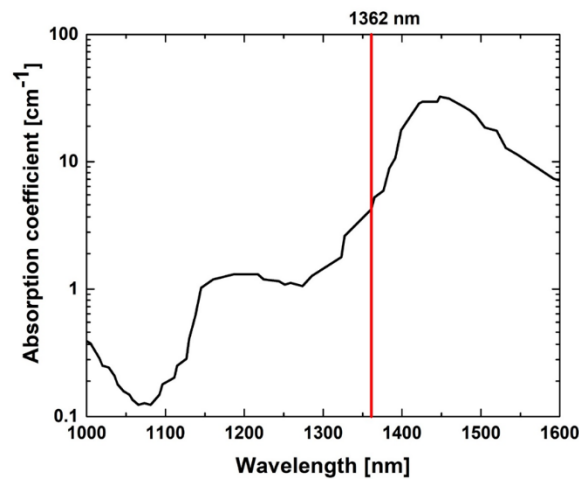


Fig. 3.5 Absorption spectrum of water in the near-infrared region.

3.4 Experiment and Discussion

Figure 3.6 shows the OCT intensity cross-sectional images of the phantoms with silica-particle volume concentrations of 0.5, 1, 2, 3, 4, and 5 vol.%. The high intensity region around the A-scan position of 150 μm was the Fresnel reflected light at the surface. Further, the intensity of the OCT cross-sectional image decreased with increase in the A-scan position because of the scattering by silica particles and the absorption by water. The decrease in the intensity became more pronounced with increase in the volume concentration because the influence of the scattering by silica particles increased. In the figure, stripe-shape intensity distribution was observed in the horizontal direction inside the phantom. This may be attributed to the strong scattering of light caused by the accumulation of silica particles in the fibrous structure of the agar.

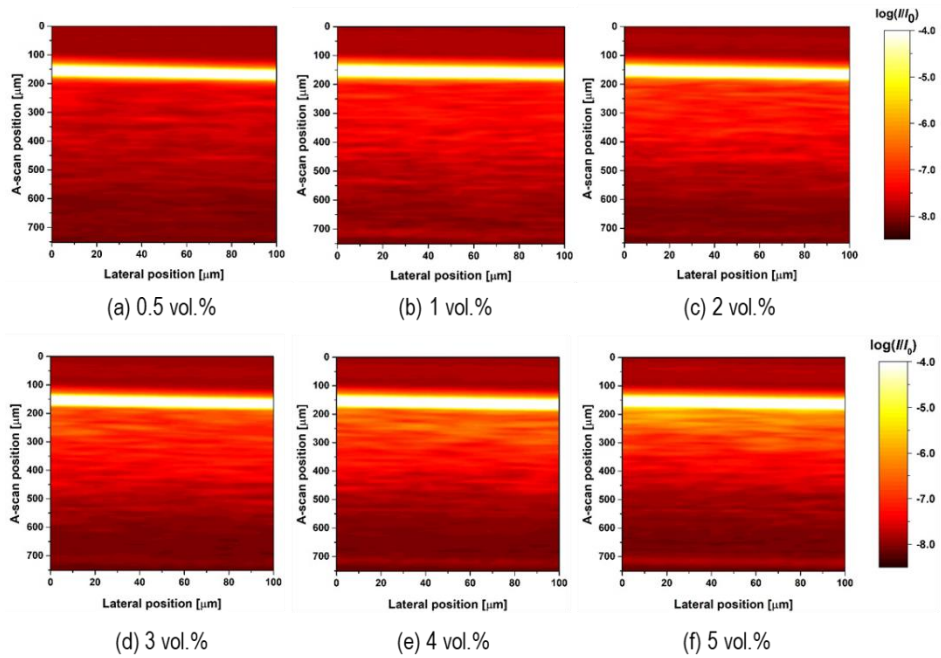


Fig. 3.6 Cross-sectional images of OCT intensity obtained from the phantom with silica-particle volume concentrations of 0.5, 1, 2, 3, 4, and 5 vol.%.

Figure 3.7 shows the A-scan intensity variations for 6 phantoms with silica-particle

volume concentrations of 0.5, 1, 2, 3, 4, and 5 vol.%. The A-scan intensity variations acquired at 20 lateral positions were averaged. In the figure, the surface position was defined as the position of the maximum A-scan intensity. Further, the natural logarithmic intensity variation of the A-scan intensity normalized by the surface intensity is plotted using a thin line. The result of linear fitting of the A-scan intensity variation in the range of 50–400 μm depth is indicated by a bold line, whose slope is equal to the attenuation coefficient obtained using Eq.(3.1). As shown in Fig. 3.7, the attenuation coefficient increased consistently with the volume concentration, which can be attributed to the increase in the scattering coefficient owing to an increase in the number density of the silica particle.

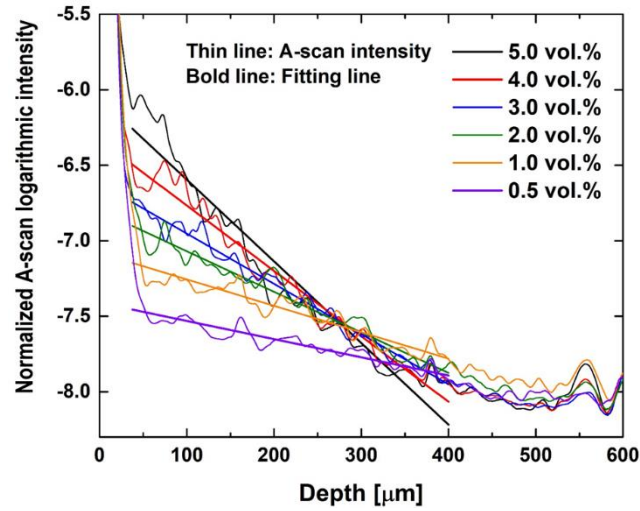


Fig. 3.7 Natural logarithmic intensity variations of the A-scan intensity normalized by the surface intensity and the lines linearly fitted in the region of 50–400 μm depth as a function of the depth for silica particle volume concentrations of 0.5, 1, 2, 3, 4, and 5 vol.%.

Figure 3.8 shows the comparison between the attenuation coefficients obtained experimentally and the theoretical values of three definitions in Eq.(3.2) calculated based on the Mie scattering theory with respect to the volume concentration of silica particles.

In the experiment, eight phantoms were prepared for each of the silica-particle volume concentrations and the mean values and standard deviations of the measured results are shown as black circles and error bars, respectively. The absorption coefficient of the water was estimated by considering the volume fraction of the water.

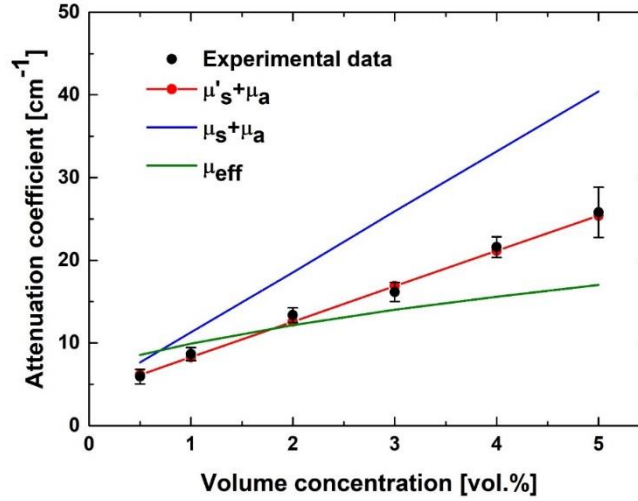


Fig. 3.8 Comparison of the attenuation coefficients measured for the phantoms with silica-particle volume concentrations of 0.5, 1, 2, 3, 4, and 5 vol.% with the three definitions of attenuation coefficients expressed as Eq. (2).

As shown in Fig. 3.8, the definition of the attenuation coefficients expressed as Eq.(3.2b) was the most consistent with the experimental results. Consequently, it was confirmed that the best definition of the attenuation coefficient was $\mu_t = \mu'_s + \mu_a$, for the measurement of the attenuation coefficient using OCT. The attenuation coefficient of Eq.(3.2b) expresses the effect of multiple scattering included in the EHF model [39,40] as the reduced scattering coefficient. Based on the optimal definition of the attenuation coefficient in this manner, it is considered that the advantage of being available for direct application of the Beer-Lambert law to the A-scan intensity distribution of OCT is quite significant.

3.5 Conclusions

This Chapter demonstrated through comparisons of the experiment with the Mie scattering theory that the optimal definition of the attenuation coefficient for OCT measurements is the sum of the reduced scattering and absorption coefficients, that is,

$$\mu_t = \mu'_s + \mu_a.$$

Based on the results in this chapter, it was clarified that OCT can be used for shape image measurement as well as the observation of distribution.

Chapter 4

Analysis of Natural Water Evaporation Process using Dual-wavelength Optical Coherence Tomography in Spectral Domain

4.1 Introduction

OCT has become one of the key technologies in the clinical field. OCT equipment suitable for observing deeper parts of living tissue have been developed using a near-infrared light source [46]. Recent OCT systems can achieve clear three-dimensional image reconstruction with high definition [47] and provide advanced feature as typified by angiography [48]. We have investigated an RGB OCT system using light-emitting diodes (LEDs) in the visible light region from a spectroscopic perspective [34,35]. Exploiting the short wavelength and low spatial coherence, the developed system possessed the capability of high-resolution and speckle-free imaging [49]. Moreover, the possibility of realizing color OCT imaging has been shown in a recent study [50]. Nakamichi et al. investigated micro-scale drug infiltration to subcutaneous tumor-implanted tissues of nude mice using a two-wavelength OCT system. The light used in the study was absorbable by the drug at a wavelength of 680 nm but not at 830 nm [51].

In Chapter 3, an OCT measurement method using a phantom, which is a high-density biological simulation such as biological tissue, and a method of observing distributions using the Lambert-Beer law were proposed. Consequently, the effectiveness of the method was demonstrated and basic knowledge was obtained.

This Chapter is focused on the investigation of dynamics of water in the tissue generated by evaporation using the SD-OCT for near-infrared SLDs. The wavelengths of the light sources were selected to be 1060 nm, which is barely absorbed by water and 1470 nm, which is absorbed by a factor of 220. The sectional intensity images were obtained as a function of the elapsed time after dropping water on the surface of tissue and the attenuation coefficients in the shallow and deep regions were analyzed employing the Beer-Lambert law introduced to the OCT system in a previous study [52].

First, the two-wavelength OCT system was verified by measuring the stem of celery, which has a high-water content and few scatterers [53]. By measuring the attenuation coefficient every hour, the change in the attenuation coefficient owing to the change in the amount of water inside the sample was evaluated. In addition, the possibility of dynamic water distribution imaging with this system was examined. Furthermore, the possibility of measuring a high-density medium such as a living body was verified. The tissue was compressed dry leaves, and was mainly composed of cellulose with a refractive-index of 1.46 at near infrared wavelengths.

The latter experimental results show that the cross-sectional image and corresponding attenuation coefficient at both the wavelengths varied in the process of evaporation; however, there no difference was observed between them contrary to expectation. The phenomenon that the light at the wavelength 1470 nm is not absorbed by water originated from the fact that the absorption cannot be accumulated owing to the lack of space in the tissue where the free water was filled. Only the scattering changed by temporal variation of the refractive-index matching effect between the hydrogen-bonded cellulose and free water around it in the process of evaporation were present. Consequently, the dynamics of water in the evaporation process was fairly well revealed via the light scattering by it

in conjunction with the refractive-index matching effect between the hydrogen-bonded cellulose and free water.

4.2 Experimental Setup and Samples

4.2.1 Two-wavelength OCT System in the Spectral Domain

Figure 4.1 shows the SD-OCT system using two SLDs (ASLD1050, ASLD1480; Amonics Ltd, Hong Kong) and Czerny–Turner spectrometers (Near infrared image sensor G10768-1024D; Hamamatsu Photonics, Japan) with central wavelengths of 1060 and 1470 nm. The spectra of the SLDs are shown in Fig. 4.2.

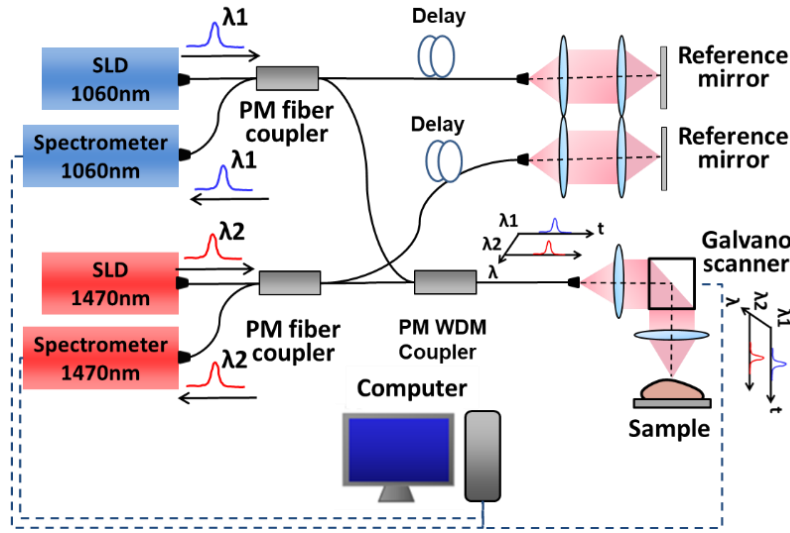


Fig. 4.1 SD-OCT system composed of two superluminescent diodes as a illumination part and spectrometers as a detection part with the central wavelengths of 1060 and 1470 nm.

The full widths at half maximum of the 1060 and 1470 nm SLDs were 42 and 52 nm, respectively, and the resolutions of the optical axis direction in the air, that is, the A-scan, were estimated to be 12 and 18 μm , respectively. Each light emitted by the SLDs was split by a polarization-maintaining (PM) coupler (PN1064R5, PN1480R5; Thorlabs, U.S.A.) into lights guided to a reference mirror and PM wavelength-division-multiplexer (WDM) coupler (PMFWDM-5506; Amonics Ltd, Hong Kong).

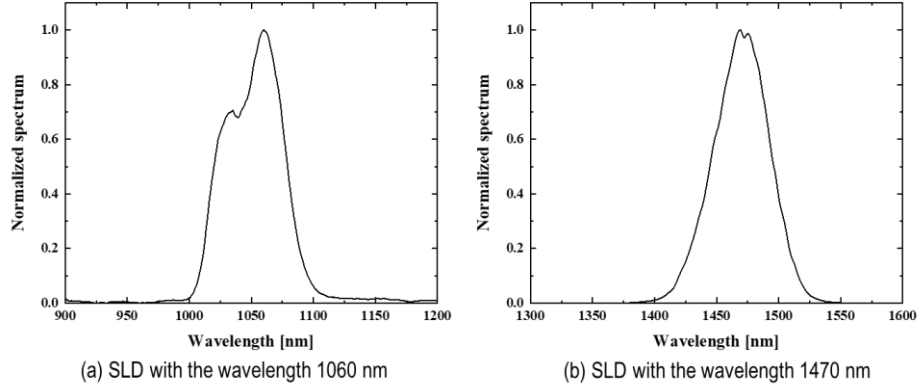


Fig. 4.2 Spectra of near-infrared SLDs with the central wavelength of (a) 1060 nm and (b) 1470 nm.

The beams with wavelengths of 1060 nm and 1470 nm multiplexed by the PM-WDM were focused on the sample by a scan lens (LSM03, Thorlabs, U.S.A.) with a 0.3 numerical aperture to form beam spot sizes of 2.2 μm and 3.1 μm , respectively. The beam spots were scanned on the sample one-dimensionally in the lateral direction by a Galvano scanner (GCM102; Thorlabs, U.S.A.). The scanning step was set as 5 μm , which was larger than the beam spot sizes, and the full scanning distance was 1 mm. The backscattered light from the sample was demultiplexed by a WDM coupler into beams with wavelengths of 1060 nm and 1470 nm and combined with the reference light by the PM coupler to obtain the spectral interference intensity. Both interference lights were separated into spectral components with resolutions of 0.11 nm and 0.14 nm in wavelength, which corresponded to the maximum measurement depths of 1.91 mm and 2.84 mm, respectively.

The intensity distribution $I(z)$ as a function of the depth z is obtained by inverse Fourier transform of the spectral interference intensity $I(k)$ as given by

$$I(z) \propto FT^{-1}[I(k)]. \quad (4.1)$$

where k is wavenumber. To compute the inverse Fourier transform of the spectral interference intensity distribution, linear sampling in k -space was performed by linearly interpolating the spectral intensity distribution as a function of the wave detected by the line sensor in the spectrometer.

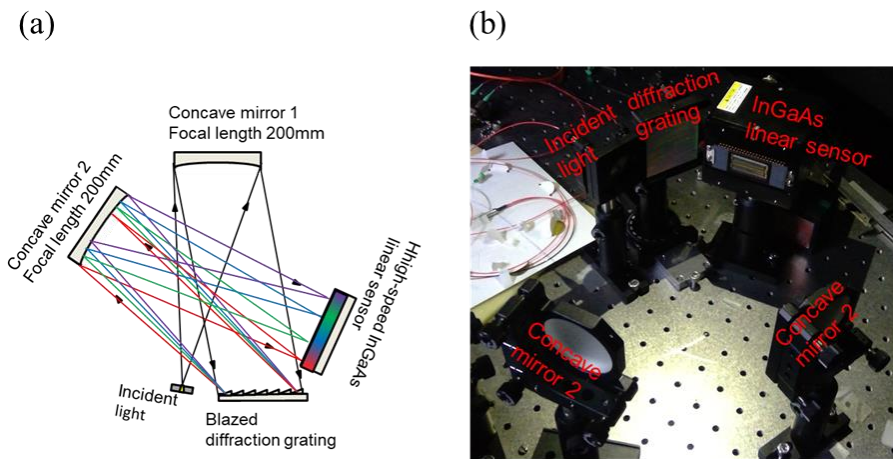


Fig.4.3 (a) Schematic diagram of light propagation and (b) setup for 1060 nm spectrometers

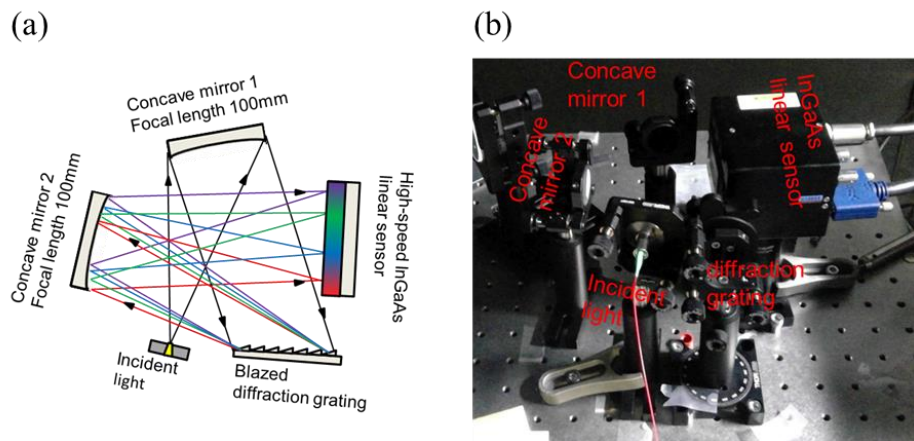


Fig.4.4 (a) Schematic diagram of light propagation and (b) setup for 1470 nm spectrometers

4.2.2 Samples used in the Experiment

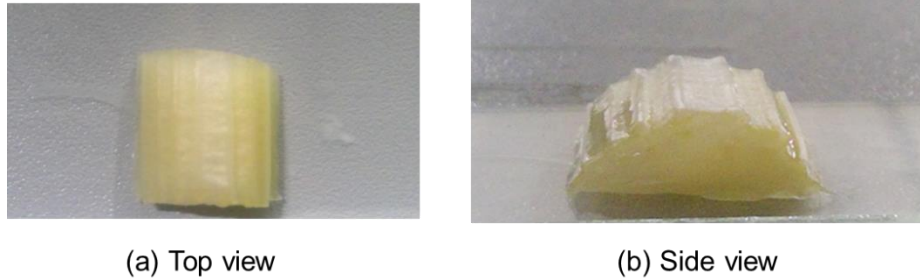


Fig. 4.5 Photographs of the celery as a sample.

Figure 4.5 shows a celery used as a sample in the experiment. Among the plant tissues, celery contains more water with a water content of 95% by volume [54]. Therefore, it is considered that water dominates the influence of light absorption on the celery tissue. Therefore, this study verified whether an image that reflects the difference in water absorption characteristics could be verified by OCT measuring the celery structure using a light source with two wavelengths that have different water absorption characteristics.

The cross-sectional image of the celery was captures every 1 hour after soaking in water for one day. Figure 4.6 shows the temporal variation of the sample weight as a function of the elapsed time. As evident, the sample weight left in a room temperature environment decreased monotonically. This indicates that the weight decreases with decrease in the water content owing to the evaporation of water.

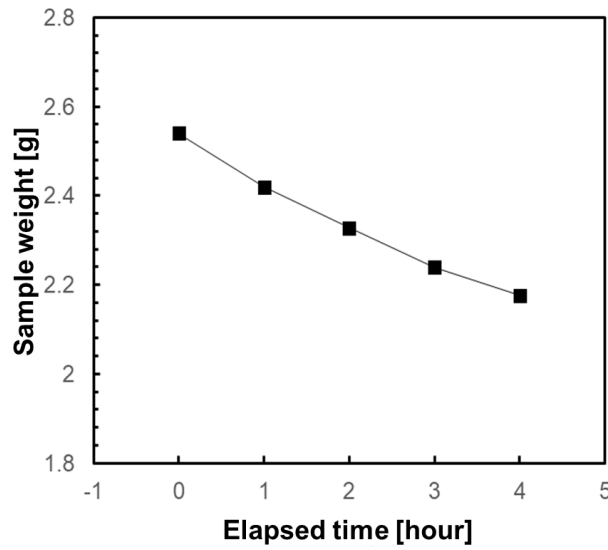


Fig. 4.6 Temporal variation of the sample weight in the celery as a function of the elapsed time.

The irradiation points were scanned using a Galvano scanner in the direction perpendicular to the optical axis, and the measurement intervals and points were 20 μm and 100 points, respectively. In addition, five different samples were measured and averaged to reduce speckle noise generated from random structures within the sample.

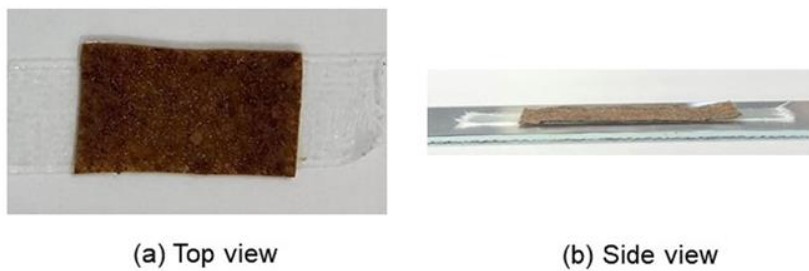


Fig. 4.7 Photographs of the sheet-shaped compressed dried leaves as a sample.

Figure 4.7 shows a sheet of compressed dry leaves used as a sample in the experiment. The species of the leaves was *Nicotiana tabacum*. Sheets were produced by finely

crushing, compressing, and re-hardening dry leaves. The sample was measured with a vernier caliper and cut into approximately 20 mm length, 15 mm in width, and 235 μm thick. It is mainly composed of cellulose and has a refractive-index of 1.46 at near infrared wavelengths. A cross-sectional image of the sheet was taken every 5 min immediately after dropping 0.4 μl of water on it. Immediately after the water was dropped, it penetrated deeply by gravity and spread over the entire sample by capillary action at the same time. And then, it evaporated from the sample surface with the elapsed time. In addition, in the entire sample, capillary action caused water to move upward against gravity. In the evaporation process in the vicinity of the surface, the evaporation interface descended and the evaporation ended when the driving capillary water potential difference between drying front and sample surface couldn't overcome the gravitational forces [55].

Figure 4.8 shows the temporal variation of the water content in the sheet as a function of the elapsed time from when the water was dropped.

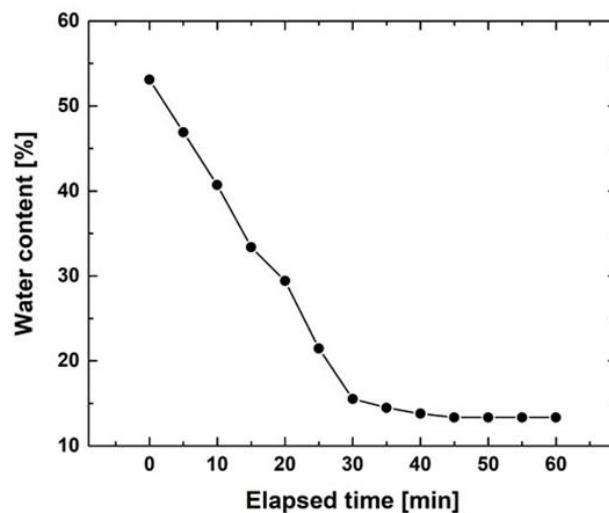


Fig. 4.8 Temporal variation of the water content in the sheet of compressed dry leaves as a function of the elapsed time from the time when water is dropped.

The water content was calculated by dividing the mass of the sheet under natural evaporation by the sum of 0.4 ml of water dropped at the initial time and 0.35 g of the completely dried sheet. As shown in the figure, the water content of a sheet left in a room-temperature environment decreases monotonically immediately after dropping water on the sheet, gradually approaches 12.3%, and then maintains approximately constant content after 30 min has elapsed. Experiments were conducted in the laboratory. The indoor air conditioning was running. The indoor temperature and humidity were about 24°C and about 20%, respectively.

4.3 Numerical Procedures of Quantitative Analysis

The intensity distribution based on backscatter interference light from the inside of the object is expressed by

$$I(z) \approx I_o(z)\mu_b(z) \cdot \exp \left[-2 \int_0^z \mu'_s(z') + \mu_a(z') dz' \right], \quad (4.2)$$

where $I_o(z)$ is the incident light intensity distribution, $\mu_b(z)$ is the backscattering coefficient of the sample, μ_s is the reduced scattering coefficient, μ_a is the absorption coefficient, and z is the depth of the scattering volume [36, 45]. The number 2 indicates that the light propagates back and forth between the surface of the sheet and the scattering volume. Here, it is assumed that the incident light intensity distribution is constant and that the spatial variation of the backscattering coefficient of the sample is small compared with the reduced scattering coefficient and the absorption coefficient [36, 45]. In addition, by taking the natural logarithm of $I(z)$ and differentiating $I(z)$ with respect to z in Eq. (4.2), the attenuation coefficient μ_t is expressed by

$$-\frac{1}{2} \frac{\partial}{\partial z} [\ln(I(z))] = \mu'_s + \mu_a = \mu_t. \quad (4.3)$$

Equation (4.3) shows that the attenuation coefficient can be calculated by measuring the backscatter interference intensity from the inside of the object at the depth. Here, μ_s changes by temporal variation of the refractive-index matching effect between the hydrogen-bonded cellulose and free water around it. The two wavelengths of the near-infrared SLDs shown in Fig.4.9 were used to investigate quantitative estimation of the attenuation coefficient in the dynamics of water evaporation.

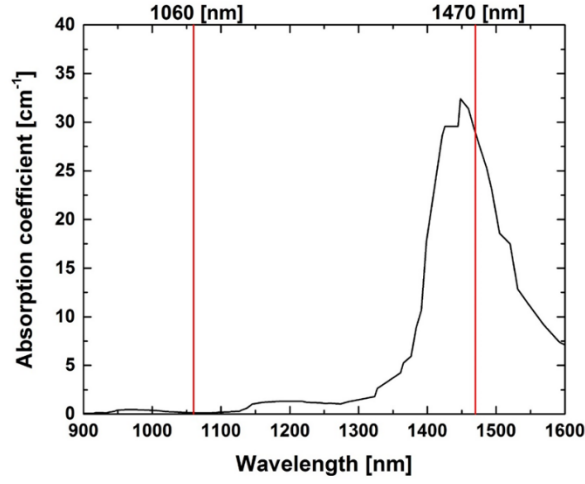


Fig. 4.9 Relation between the absorption coefficients of water and the central wavelengths of two SLDs used in the dual-wavelength SD-OCT shown in Fig. 4.1.

As the absorption coefficients of water at the wavelengths of 1060 nm and 1470 nm are 0.13 cm^{-1} and 28.85 cm^{-1} , respectively, the attenuation coefficients are approximately given by

$$\mu_t^{1060} = \mu_a^{1060} + \mu_s'^{1060} \approx \mu_s'^{1060}, \quad (4.4)$$

and

$$\mu_t^{1470} = \mu_a^{1470} + \mu_s'^{1470} \approx \mu_a + \mu_s'^{1470}, \quad (4.5)$$

where $\mu_a^{1060} \approx 0$, and $\mu_a = \mu_a^{1470}$. It may therefore be expected that the dynamics of water inside the tissue in the natural evaporation process can be observed via μ_a by comparison between μ_t^{1470} and μ_t^{1060} .

4.4. Experimental Results and Discussions

4.4.1 Water Distribution Imaging Inside Celery

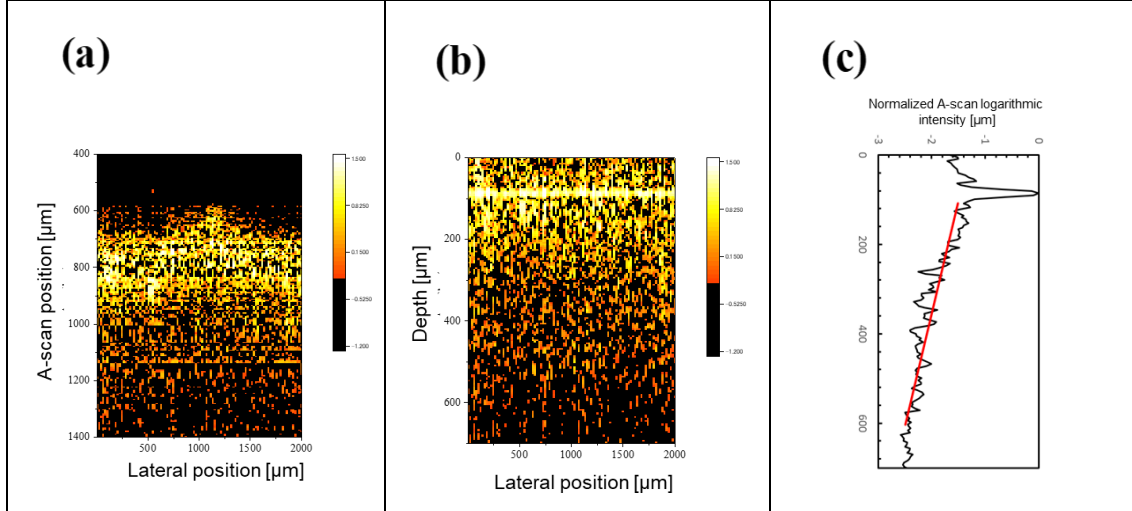


Fig. 4.10 (a) Tomographic imaging using OCT. (b) Surface-normalized tomographic image. (c) Distribution of averaging backscattered light intensity with depth as a variable.

Figure 4.10 (a) shows a tomographic image obtained using OCT, and Fig. 4.10 (b) shows a surface-normalized tomographic image obtained by searching the sample surface and matching the surfaces. Figure 4.10 (c) shows the average backscattering intensity distribution with depth as a variable, which was obtained by normalizing based on incident intensity, averaging in transverse direction, and logarithmic processing. This averaged backscattering intensity distribution was subjected to least squares fitting processing inside the sample excluding the Fresnel reflected light part. The slope of the intensity is equal to the attenuation coefficient and should be linear from Eq.(3.1) [45]. As shown in Fig.4.1 (c), the attenuation coefficient increased linearly with the propagation of light. This result indicates that the attenuation coefficient can be

calculated from the OCT measurement results. Thus, by calculating the attenuation coefficient using these processes, the water distribution can be observed.

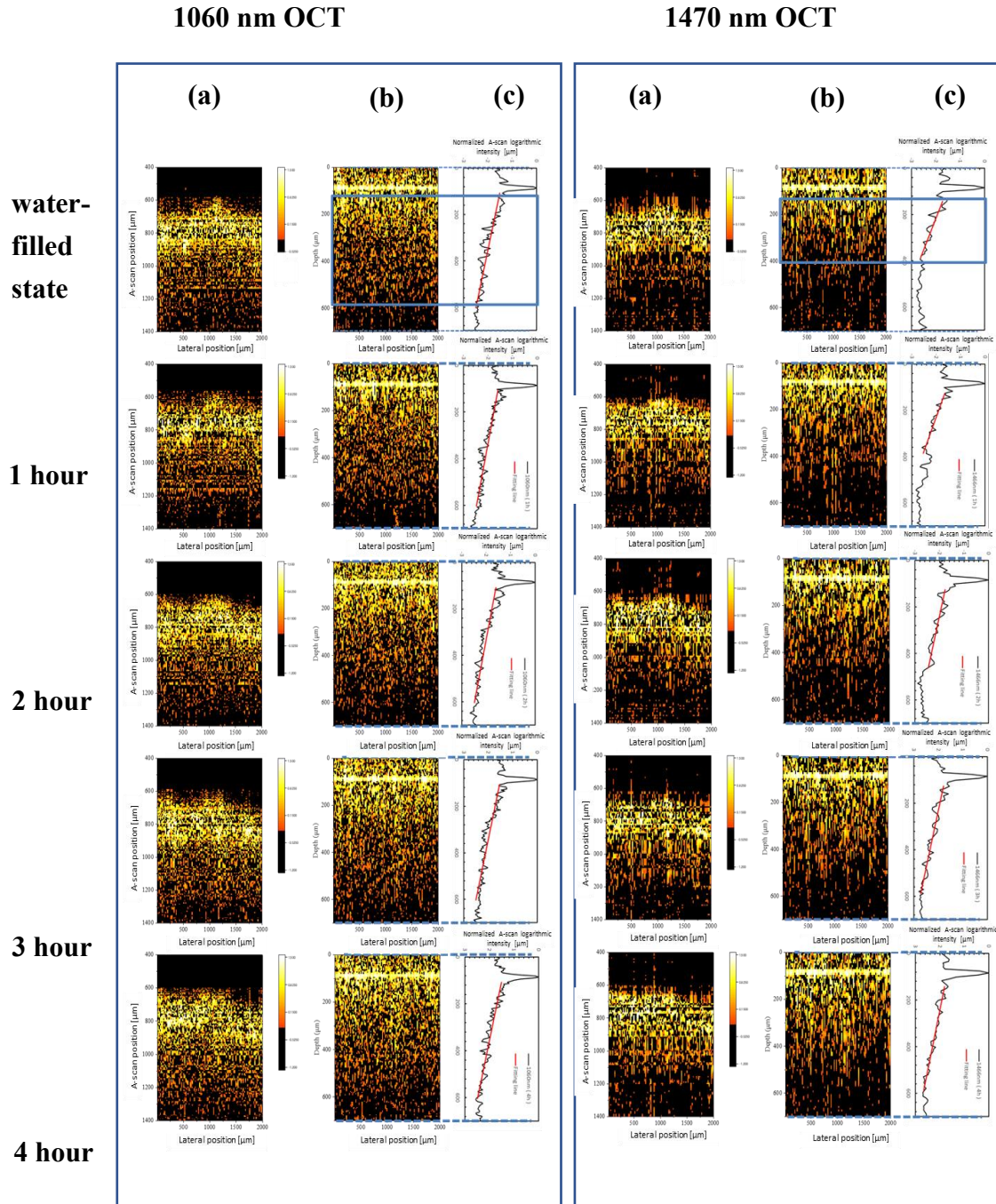


Fig. 4.11 Tomographic imaging using 1060 nm and 1470 nm OCT

Figure 4.11 show the tomographic imaging measured using 1060 and 1470 nm OCT from the time when water was filled till the lapse of 4 h. Figures 4.11 (a), (b), and (c) show the tomographic imaging, surface-normalized tomographic image, and the distribution of averaging backscattered light intensity with depth as a variable. The change in brightness at a depth of 800 μm for each image is the boundary between the air and the sample surface, which is the Fresnel reflected light from the sample surface. In the tomographic image of 1060 nm OCT, it was confirmed that the brightness was high as a whole regardless of the elapsed time. Moreover, the light was not attenuated and reached deep inside. This indicates that there is no effect of water absorption at wavelengths where water absorption is minimal. In the deep part of the tomographic image of 1470 nm OCT, it was confirmed that the brightness was the lowest in the water-filled state. In addition, the light was attenuated and could not reach deep. This indicates that the influence of water absorption is large at wavelengths where water absorption is maximum. Further, focusing on the change with time, it can be confirmed that the light reached deeper with the elapsed time in the 1470 nm OCT. This is because the water in the celery evaporated and the water content decreased.

These results confirmed that 1060 and 1470 nm OCT changed differently depending on the water content. Therefore, the amount of absorbed water can be detected from the difference between the 1060 and the 1470 nm OCT images, indicating the possibility of water content imaging.

Next, an evaluation was performed based on the distribution of the average backscattered light intensity. The red line indicates the result of linear fitting in the range where the backscattered light could be detected for the intensity change. The fitting straight line indicates that there was no change in the slope with the elapsed time in the 1060 nm OCT,

with the slope being small as a whole. However, in 1470 nm OCT, the inclination was large when filled with water, and it decreased with elapsed time. A large slope implies a large decrease in backscattered light, and a large amount of attenuation inside the sample. The change in attenuation is owing to absorption by water.

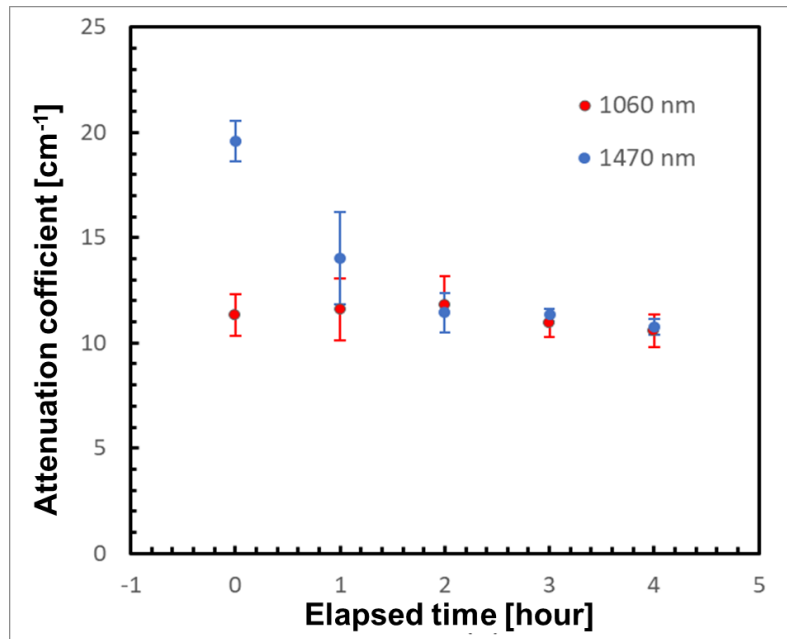


Fig. 4.12 Time course of attenuation coefficient inside the sample at 1060 and 1470 nm

Figure 4.12 shows the time course of the attenuation coefficient inside the sample at 1060 and 1470 nm. The attenuation coefficient was obtained by averaging each attenuation coefficient obtained from 5 samples, and at that time, the error bars were calculated. In Fig. 4.12, it is evident that the changes in the attenuation coefficient over time differed for the 1060 and 1470 nm cases. As mentioned in Chapter 4.1, in celery with less scattering, the difference in attenuation coefficient between the two wavelengths was the difference in absorption coefficient by water. The difference between the attenuation coefficients of 1060 and 1470 nm was the largest at 0 min,

decreased with elapsed time, and disappeared after 3 h. This is similar to the change in celery weight owing to water evaporation shown in Fig. 4.6.

Based on these results, we demonstrated the water content imaging in plant tissues with this system.

4.4.2 Water Distribution Imaging Inside Sheet of Compressed

Dry Leaves

Cross-sectional images of the sheet of compressed dry leaves were acquired in the dry state and every 5 min from the time when water was dropped until 90 min had elapsed. Figures 4.13 and 4.14 show the cross-sectional images for illuminating light with central wavelengths of 1060 nm and 1470 nm, respectively. The scale of color bars was the same for all graphs. In each figure, the surface shape of the tomographic image changed with the elapsed time due to the change of water distribution in the medium by drying. The surface shapes at 1060 nm and 1470 nm OCT were slightly different, despite the measurements were performed at the same time. This is considered to be caused by the lateral color shift of the objective lens that affects the lateral focal positions. Figures 4.15(a) and (b) show the intensity variation as a function of depth corresponding to the images Figs. 4.13 and 4.14, respectively. These were obtained by averaging A-scan intensity variations at 200 lateral positions.

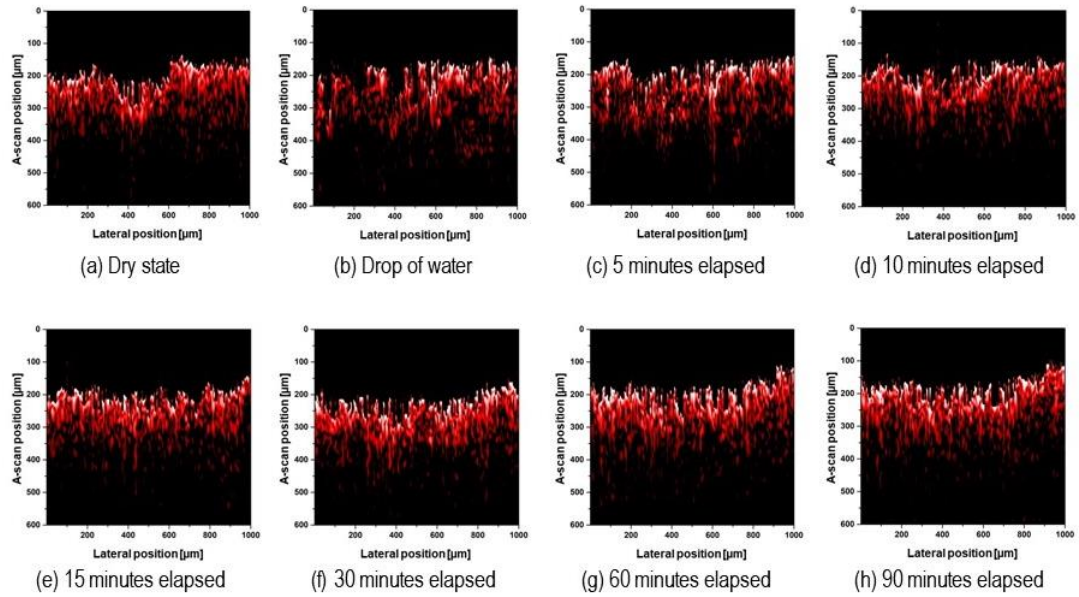


Fig.4.13 Cross-sectional images of the sheet of compressed dry leaves from the time when water was dropped to 90 minutes elapsed. The wavelength of the illuminating light was 1060 nm.

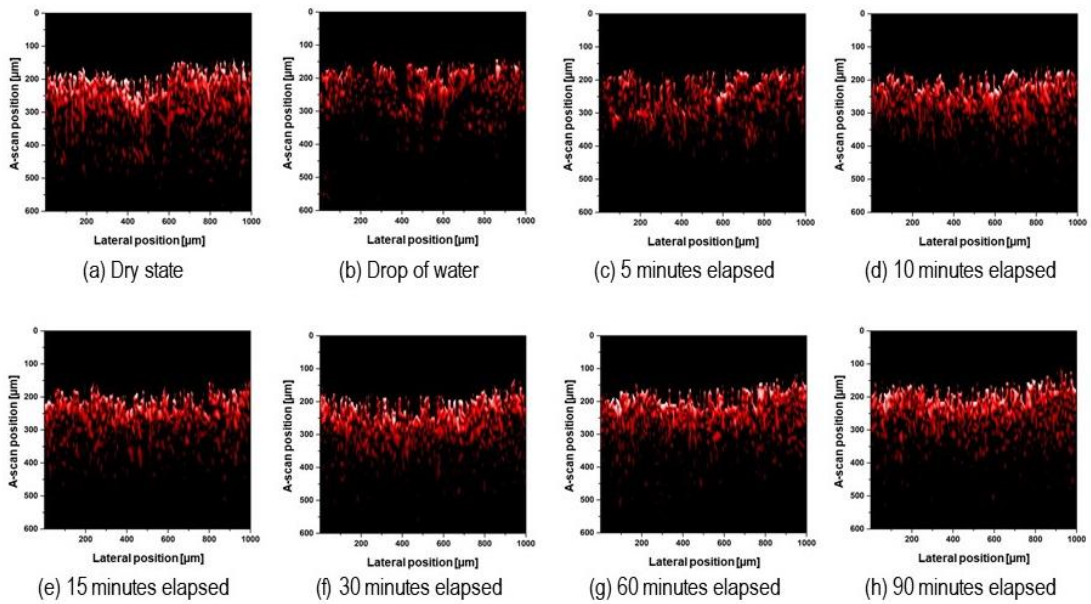


Fig. 4.14 Cross-sectional images of the sheet of compressed dry leaves from the time when water was dropped to 90 minutes elapsed. The wavelength of the illuminating light was 1470 nm.

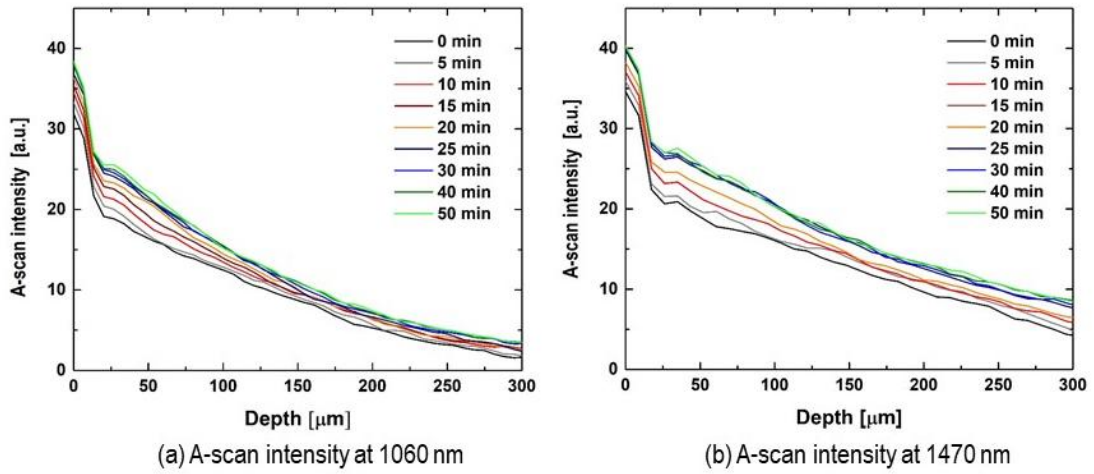


Fig. 4.15 A-scan intensity variations as a function of the depth from the surface for 9 different elapsed times. They were obtained from the cross-sectional images shown in Figs.4.13 and 4.14.

In the figures, the attenuation of intensity changed at 25 μm and 150 μm depths from the sample surface at each elapsed time. This indicates that the state of water distribution is different in each region.

The discussion may be divided into three regions of depth, namely in the vicinity of the surface, in the shallow region from 25 μm to 150 μm , and in the deeper region beyond 150 μm . Figures 4.13-4.15, the intensity in the vicinity of the surface was highest in the dry state, decreased at the time when the water was dropped, gradually increased from 5 to 25 min, and approached the intensity in the dry state after 30–90 min. Fig.4.16 shows the variations in surface intensity shown in Fig.4.15 as a function of the elapsed time. In the experiment, 10 samples were prepared. The mean values and standard deviations of the measured results were depicted by circles and error bars, respectively. In the figure, the intensity variations are normalized by the intensities in the dry state. The minimum

value of the normalized surface intensity occurred at the time when the water was dropped because the water filled in the surface so that the scattering effect from the surface was minimized due to the decrease in the refractive-index difference from that between cellulose and air to that between cellulose and water.

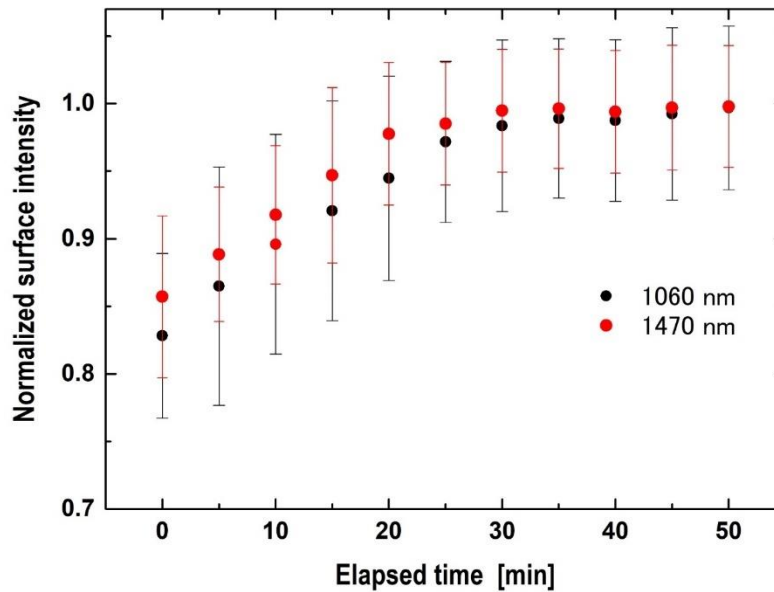


Fig. 4.16 Temporal variations of the surface intensities at the wavelengths of 1060 and 1470 nm. The surface intensity variations were normalized by the intensities in the dry state.

As evaporation progressed and the cellulose became exposed to air, the scattering intensity increased consistently with the elapsed time and approached the intensity of the dry state after 30–50 min. The surface scattering intensity from 50 min is similar to initial dry conditions. In the figure, the surface intensity at the wavelength of 1470 nm was larger than that at 1060 nm. This was due to the fact that the efficiency of the spectrometers were about 18% better at 1470 nm than 1060 nm, despite the experiments being conducted under the condition of the same peak intensity of illumination at both 1060 nm and 1470 nm. Fig.4.17 shows the temporal variations of

the attenuation coefficients in the shallow and deeper regions as a function of the elapsed time. By applying the linear least-squares fitting to the A-scan intensity change in each of the shallow region and the deep region, the attenuation coefficient shown in the Eq. (4.4) was calculated. In the experiment, 10 samples were prepared. The mean values and standard deviations of the measured results were depicted by symbols and error bars, respectively. Here, we explain the change of attenuation coefficient in Fig. 4.17. Immediately after the water was dropped, the attenuation coefficient in the shallow region indicated the minimum value. This is because the scattering effect from the surface is reduced in the water-filled state. The dropped water penetrates the sheet of compressed dry leaves due to the capillary action and gravity [55]. After the water penetrates, hydrogen-bonded water is produced by hydrogen-bonding water and the hydroxy group of cellulose, and free water fills around it when the hydrogen bonds are saturated [56]. As the refractive-index of the hydrogen-bonded cellulose may decrease from 1.46 so that the refractive-index matching effect between cellulose and water becomes more effective, the scattering intensity decreases notably after the water is dropped. As evaporation progresses in the vicinity of the surface, free water rises from the shallow region to the surface by capillary action. After 5 min have elapsed, the attenuation coefficient increased consistently with the elapsed time. This is due to the evaporation of the free water. The evaporation becomes faster than the movement of the water from the deep region, so the gaps between the cellulose become filled with air and the refractive-index matching effect is lost. As the scattering intensity reached its maximum, the attenuation coefficient reached a constant maximum value from 40 min. In contrast, the attenuation coefficient at 1470 nm changed differently in the deep region. Because water permeates by gravity, the deep region rather than the shallow

region becomes filled with free water. Because the absorption coefficient of water is large at 1470 nm, the light intensity decreases notably after the water is dropped. Therefore, the attenuation coefficient at 1470 nm reached its maximum value in the deep region. As evaporation progresses, free water rises from the deep to the shallow region by capillary action. From 5 min to 40 min, the attenuation coefficient in the shallow region increased due to the loss of the index matching caused by the evaporation of the free water, whereas the attenuation coefficient at 1470 nm decreased with the elapsed time. As the absorption of water reached a minimum, the attenuation coefficient reached a constant minimum value from 40 min. In contrast, the change in the attenuation coefficient at 1060 nm was similar to that in the shallow region and increased with elapsed time. The difference in attenuation coefficients between 1060nm and 1470 nm is due to the absorption of light by free water. Therefore, because the amount of free water decreases by evaporation, the difference between the attenuation coefficients of each wavelength decreases with the elapsed time. However, such changes in the attenuation coefficient due to water absorption are small even in the deep region where water remains. It was expected in the previous section that only the scattering by cellulose was generated at 1060 nm and not only scattering by cellulose but also absorption by water were generated at 1470 nm.

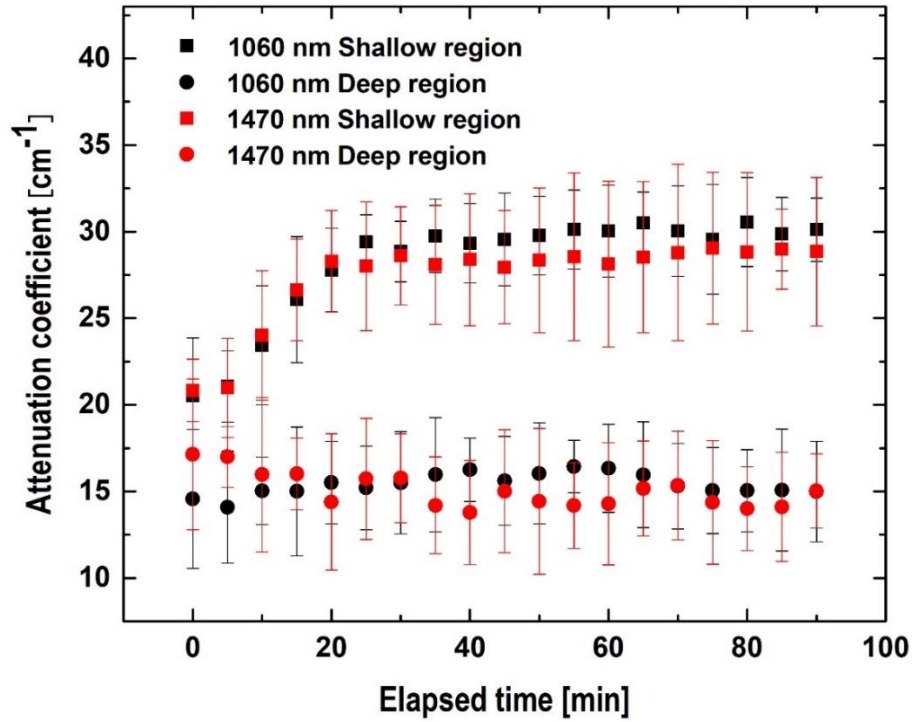


Fig.4.17 Temporal variations of the attenuation coefficients in the shallow and deep regions at the wavelengths of 1060 nm and 1470 nm.

However, Fig.4.17 shows that the difference between the attenuation coefficients at 1060 nm and 1470 nm is small, indicating that cellulose scattering is dominant. This may be attributed to the fact that the absorption is not accumulated enough due to the low volume fraction of free water in the tissue. The absorption of water certainly affects the attenuation coefficient for the samples that possess a large volume fraction of water, a celery stalk [53], and the phantom in which the suspension of silica particles was solidified by agar [52]. Nevertheless, it is concluded that the quantitative analysis results for each region of the cross-sectional images shown in Figs. 4.13 and 4.14 clearly indicate the dynamics of water inside the compressed dry leaves in the process of evaporation by considering them together with the refractive-index matching effect between the hydrogen-bonded cellulose and free water.

4.5 Conclusions

This Chapter focused on the development of a two-wavelength SD-OCT system in the near-infrared region and its application to cross-sectional imaging and observation of distribution of the natural evaporation. The wavelengths of the light sources were selected to be 1060 nm, which is not absorbed by water, and 1470 nm, which is absorbed by a factor of 220.

First, the two-wavelength OCT system was verified by measuring the stem of celery, which has a high-water content and few scatterers. It was confirmed that the change in the amount of water measured by the weigh meter and the change in the difference between the attenuation coefficients of the two wavelengths acquired by this system were similar. Thus, these results were used to demonstrate the water content imaging in plant tissues with this system.

Second, the effect of the water absorption and the scattering on the attenuation coefficient in the dense medium was examined using a two-wavelength SD-OCT system in the near-infrared. The wavelengths of the light sources were selected to be 1060 nm, which is not absorbed by water, and 1470 nm, which is absorbed by a factor of 220. Experimental results showed that the attenuation coefficient in dense medium was more affected by scattering than by water absorption. The phenomenon that the light at a wavelength of 1470 nm is not absorbed by water can be attributed to the fact that the absorption cannot be accumulated due to the lack of space in the tissue where it is filled by the free water. The scattering changed by temporal variation of the refractive-index matching effect between the hydrogen-bonded cellulose and free water around it in the process of evaporation. As a result, we showed the possibility of measuring the dynamics of water in the evaporation process through light scattering by considering them together

with the refractive-index matching effect between hydrogen-bonded cellulose and free water. It was concluded that the SD-OCT was a potentially practical and useful tool to visualize and quantitatively analyze natural phenomena that have never before been observed.

Chapter 5

Analysis of Water Evaporation Process by Temperature Control System for Peltier Element using Near-infrared Optical Coherence Tomography in Spectral domain

5.1 Introduction

Based on the results of Chapter 4, it was confirmed that in a high-density medium with a high refractive-index, absorption is not accumulated owing to the lack of space in the tissue filled with free water, and that scattering is dominant. In addition, it was confirmed that a dynamic image of water content is possible with 1470 nm OCT alone.

In this Chapter, based on the research results presented till now, we verified the dynamic imaging and observation of distribution of the evaporation process employing a method that combined the 1470 nm OCT and Lambert-Beer law. The sample was a sheet-shaped compressed dried leaf used in Chapter 4. The evaluation of the evaporation process was performed by natural and short-time drying using a heat-system, and the observation of the evaporation process imaging of water and the real-time visualization of the evaporation process were verified.

5.2 Experimental Setup and Samples

5.2.1 Real-time Near-infrared SD-OCT System

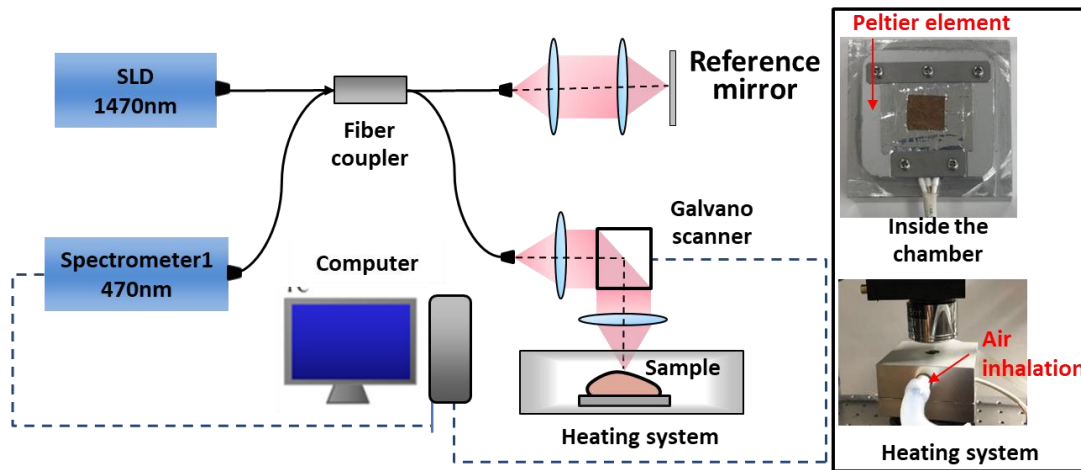


Fig. 5.1 Real-time Near-infrared SD-OCT system with the central wavelengths of 1470 nm.

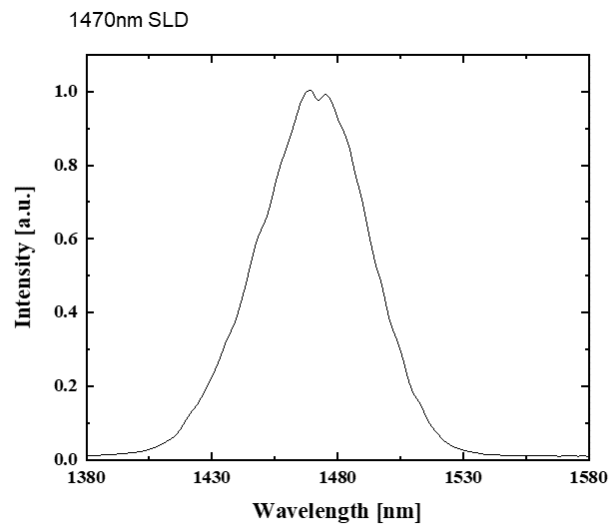


Fig. 5.2 Spectra of near-infrared SLDs with the central wavelength of 1470 nm.

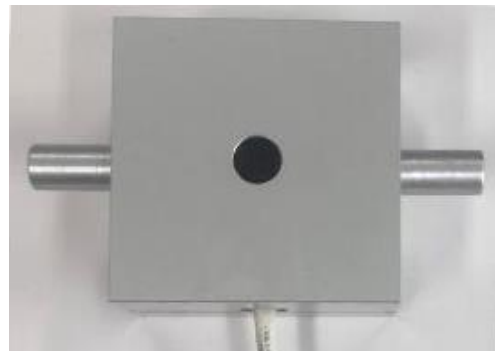
Figure 5.1 shows the optical system of the Real-time Near-infrared SD-OCT system used in this experiment. The light emitted from the SLD light source was divided among the reference mirror and sample sides via the fiber coupler, and the sample side was irradiated to the sample through the Galvano scanner. The sample containing water was installed in a heating system and the drying time could be adjusted arbitrarily. The reflected and backscattered light from the reference mirror and sample returned to the fiber coupler and functioned as interference light, which was then detected by the spectroscope as the interference spectra. The Galvano scanner performed a one-dimensional sweep of the irradiation points on the sample in the direction perpendicular to the optical axis at intervals of 5.0 μm , and acquired tomographic images. The spectrum of the SLD light source is shown in Fig. 5.2. The central wavelength and wavelength bandwidth of the light source were 1470 nm and 52 nm, and the coherence length representing the resolution in the optical axis direction was 18 μm , obtained using Eq. (2.18). Further, the numerical aperture of the F θ lens was approximately 0.3, and the resolution in the direction perpendicular to the optical axis was 3.0 μm .

The resolution of the 1470 nm spectrometer was 0.14 nm and the measurable depth was 2.84 mm, obtained using Eq. (2.21). Further, to reduce speckle noise generated from the random structure in the sample structure, the sample was measured 10 times in the horizontal direction of the optical axis and then averaged. The heating-system is shown in the Fig. 5.3. The Peltier element was used as the heater for the heating system, with a maximum output and heating rate of 400 $^{\circ}\text{C}$ and 150 $^{\circ}\text{C}/\text{s}$, respectively. Thereafter, a sample was placed on this heater, housed in a chamber, and heated. On the side of the chamber, the functions of discharging water vapor and inhaling air were attached. In the chamber, if the sample moves, the same position cannot be measured, thus, the sample

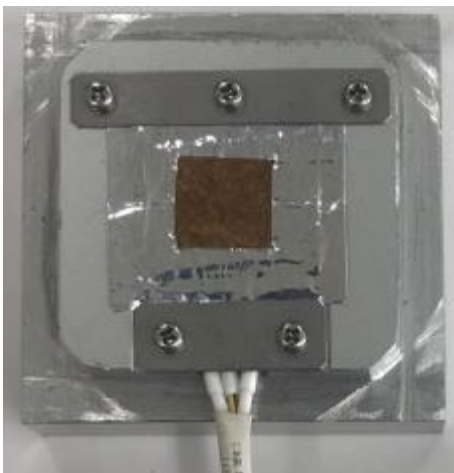
was covered with aluminum foil with holes and screwed with plate-shaped ceramic to fix the sample. This system was used to visualize dynamics of the evaporation process in/from the tissue.



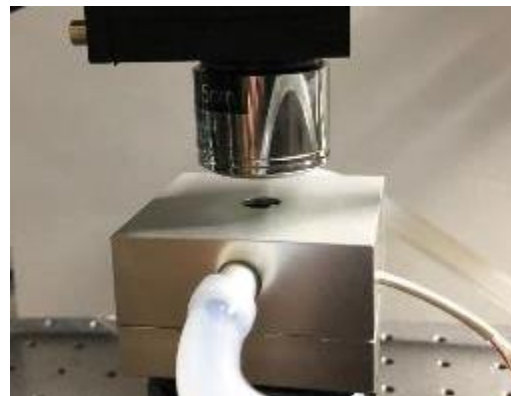
(a) Peltier element



(b) Top of the chamber



(c) Inside the chamber



(d) External view

Fig. 5.3 Heating System

5.2.2 Sheet of Compressed Dry Leaves and Evaporation Process

The sample used in this experiment was a sheet-shaped compressed dried leaf, which was the same as that used in Chapter 4. Sheet-shaped compressed dried leaves and the schematic are shown in Fig. 5.4. The cross-sectional images of the tissue in the process of evaporation were considered as a function of elapsed time after dropping the water droplet. The evaluation of the evaporation process was performed based on natural and short-time drying using a heating system. In addition, the observation of the evaporation process imaging of water and the real-time visualization of the evaporation process were verified. In natural drying, water droplets were dropped on the sheet of compressed dry leaves, and then the leaves were dried in the air. Figure 5.4 shows the change over time in the moisture content in the sheet of compressed dry leaves measured with a weight measuring instrument.

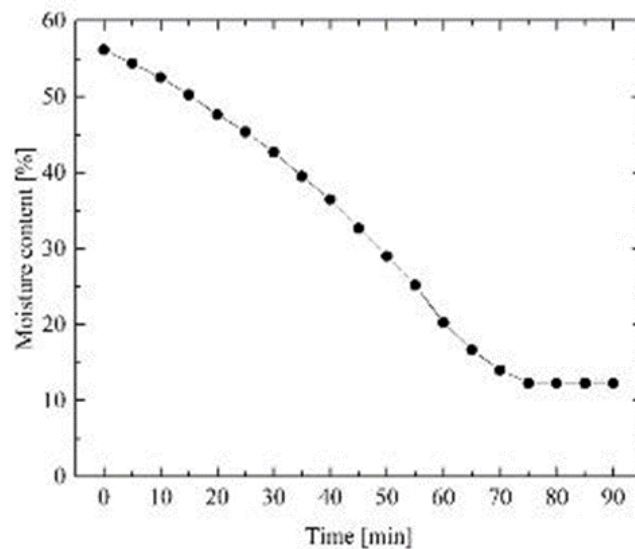


Fig. 5.4 Temporal variation of the water content in the sheet of compressed dry leaves as a function of the elapsed time from the time when water is dropped in natural drying.

The change in water content continued to decrease significantly up to 75 min, disappeared after 90 min, and then the only water left in the dried leaves that were compressed into sheets was the water that it originally contained. Thus, the water content imaging by OCT measured the same position every 5 min from immediately after the water was dropped up to 90 min. In contrast, in the short-time drying case using the heating-system, the sheet of compressed dry leaves were dried in a short time by dropping water in a state of being heated to 80 °C. Figure 5.5 shows the change over time in the moisture content in the sheet of compressed dry leaves measured with a weight measuring instrument.

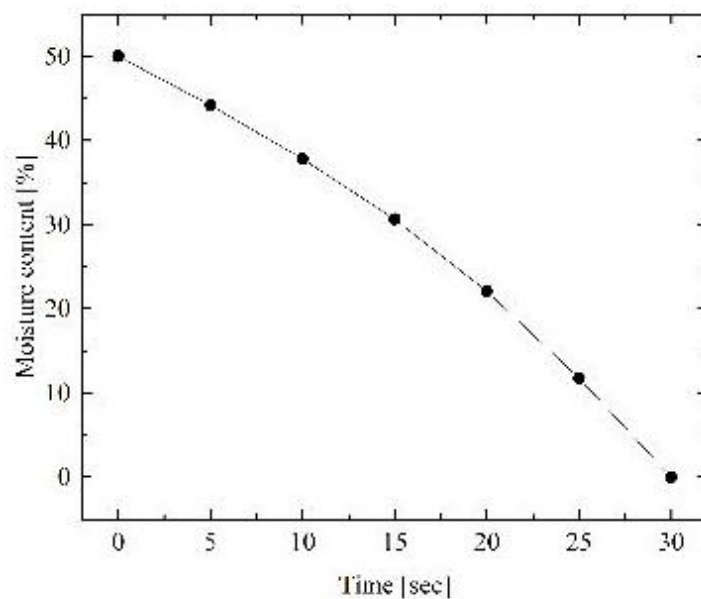


Fig. 5.5 Temporal variation of the water content in the sheet of compressed dry leaves as a function of the elapsed time from the time when water is dropped in forced drying.

Immediately after dropping the water droplets, the water content reached a maximum of 50 %, and then decreased with elapsed time. After 30 s, all the water evaporated. Based

on this, in the water content imaging by OCT, the same position was continuously measured every 5 s from immediately after the water was dropped up to 30 s. The change in water content continued to decrease significantly up to 30 s, disappears after 30 min, and then the water left in the dried leaves that are compressed into sheets also evaporated.

5.3 Experimental Results and Discussions

5.3.1 Evaporation Process over Time in Natural Drying

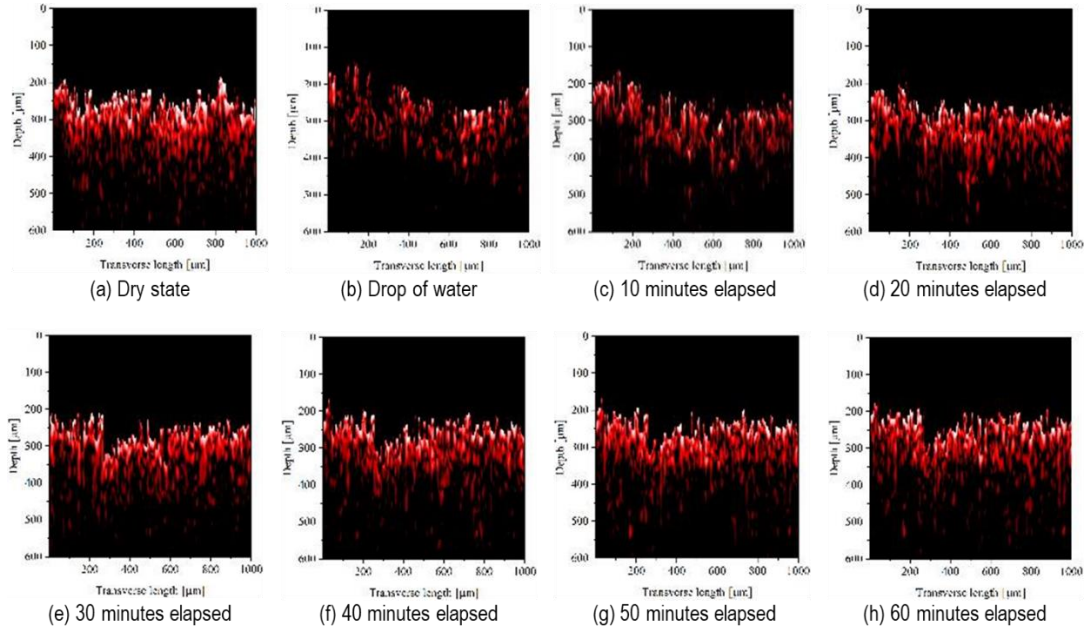


Fig. 5.6 Cross-sectional images of the sheet of compressed dry leaves from the time when water was dropped up to 60 min. The wavelength of the illuminating light was 1470 nm.

The cross-sectional images of the sheet of compressed dry leaves were acquired in the dry state and at every 10 min from the time when water was dropped up to 60 min. Figure 5.6 shows the cross-sectional images for illuminating lights with the central wavelength of 1470 nm. The change in brightness near the depth of 200 μm of each image is the boundary between the air and sample surface, which is the Fresnel reflected light from the sample surface. It can be confirmed that the tomographic image of OCT exhibited a high brightness as a whole in the dry state, whereas, the brightness was greatly reduced in the water-filled state. The first reason for this difference in brightness can be attributed to the index matching that occurred in the water-filled state and the backscattered light

becoming weaker. Index matching is a phenomenon wherein reflected light is weakened by sandwiching a medium with a different refractive-index between a mediums on the incident and target sides. Second, as 1470 nm is a wavelength with a large water absorption coefficient, light was absorbed by water in a water-filled state, and thus the backscattered light decreased. Focusing on the time course of the tomographic image, it was confirmed that the brightness increased with elapsed time. This indicates that the difference in the brightness value of the tomographic image can be confirmed depending on the evaporation state of the water contained in the sample.

By calculating the attenuation coefficient using a method that combines the OCT measurement and Lambert-Beer law, the evaporation process of water in a sheet of compressed dry leaves was-evaluated.

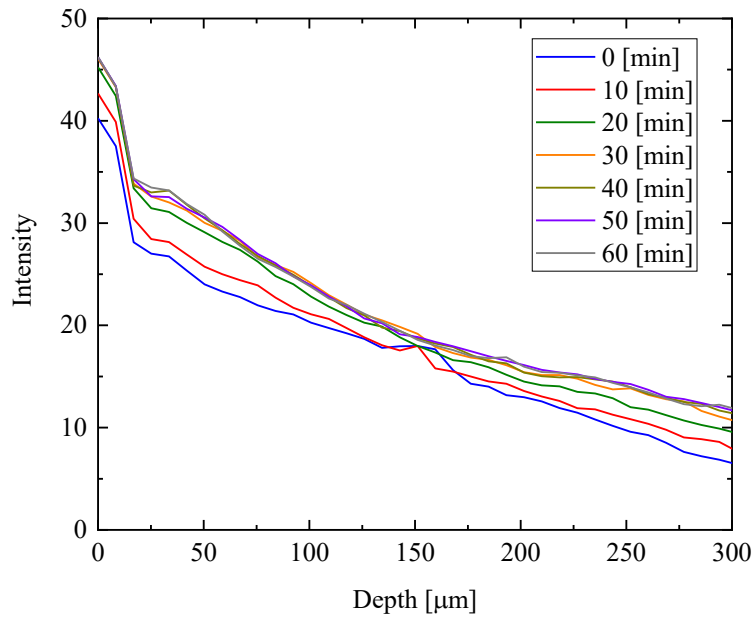


Fig. 5.7 Distribution of averaging backscattered light intensity with depth as a variable.

Figure 5.7 shows the distribution of the averaging backscattered light intensity with the depth as a variable calculated from the tomographic image and the time course of attenuation coefficient inside the sample. Each calculation was calculated by the technique established in a previous study. In the average backscattered light intensity distribution, the backscattered light intensity was the lowest at 0 min on the sample surface and inside, and it increased with time. The low backscattered light intensity in the state of being filled with water can be attributed to the lowering of the backscattered light intensity by the index matching and the large absorption of water. Further, the intensity increased as the effect of absorption and index matching decreased with decrease in the water content owing to water evaporation.

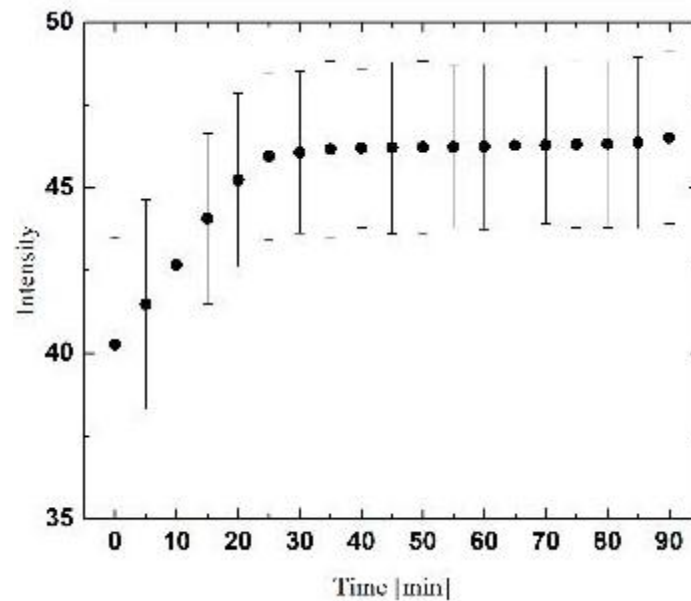


Fig. 5.8 Temporal variations of the surface intensities. The surface intensity variations are normalized by the intensities in the dry state.

Figure 5.8 shows the variations of the surface intensity shown in Fig. 5.7 as a function of the elapsed time. The intensity variations were normalized by the intensities in the dry state. The normalized surface intensity yielded minimum values at the time when water was dropped because water was filled on the surface such that the scattering effect from the surface was minimum owing to the decrease in the refractive-index difference between cellulose and air to that between cellulose and water.

Figure 5.9 shows the time course of the attenuation coefficient inside the sample.

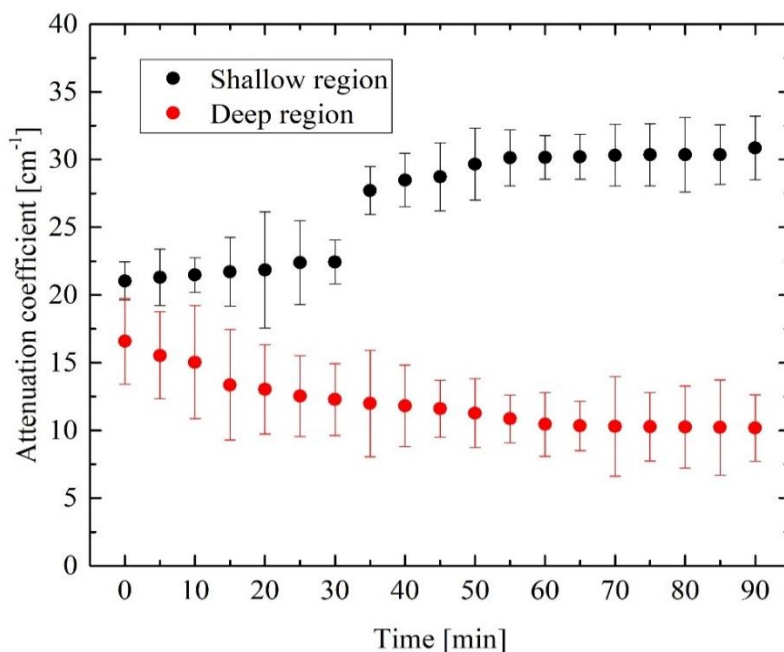


Fig. 5.9 Time course of attenuation coefficient inside the sample.

The attenuation coefficients were obtained by averaging the attenuation coefficients from each of the 10 samples, and the error bars were calculated. The attenuation coefficient changed in different manners in the shallow and deep regions, which is owing to the absorption of water. After the water was dropped, the attenuation coefficient yielded the minimum and maximum values in the shallow and deep regions of the sample. This

indicates that the influence of absorption and scattering on the attenuation coefficient were small and dominant, respectively, in the shallow region where the water content was low and vice versa in case of the deep region, where the water content was high. Therefore, a large amount of water in the shallow region of the sample, results in a large effect of the refractive-index matching and the equivalent scattering coefficient becomes small. Consequently, the attenuation coefficient decreases. However, when the amount of water in the deep region of the sample is large, the influence of water absorption increases, such that the attenuation coefficient increases. Next, in the shallow region, the attenuation coefficient increased with elapsed time. The increase in the attenuation coefficient increased particularly after 30 min. This indicates that the movement of water from the deep region could not match with the evaporation of the shallow region after 30 min. However, after 50 min, the attenuation coefficient was constant. indicating that the shallow regions of the sample were mostly dry. In contrast, in the deep region, the attenuation coefficient decreased until 30 min. This indicates that free water decreased in the deep region. The change of the attenuation coefficient decreased after 30 min indicating that there was minimal free water in the deep regions. After 30 min, the amount of water supplied from the deep region of the sample decreased with respect to the evaporation of water, such that the water content decreased and the attenuation coefficient increased in the shallow region of the sample. At that time, there was almost no free water in the deep region.

Based on these results, the evaporation process in the sample is discussed. Figure 5.10 shows the image of the water evaporation process. The water in the sample was accumulated in the deep region immediately after the water was dropped. Thereafter, the water in the sample was dried on the surface and supplied from the deep region to the

shallow region via capillary action [55, 57-58]. After 30 min, the amount of water supplied from the deep region of the sample decreased with respect to the evaporation of water, such that the water content decreased and the attenuation coefficient increased in the shallow region of the sample. At that time, there was almost no free water in the deep region. Thus, based on the above results, the possibility of a technique that can visualize the evaporation process in the biological tissue using OCT and beer-lambert law was shown.

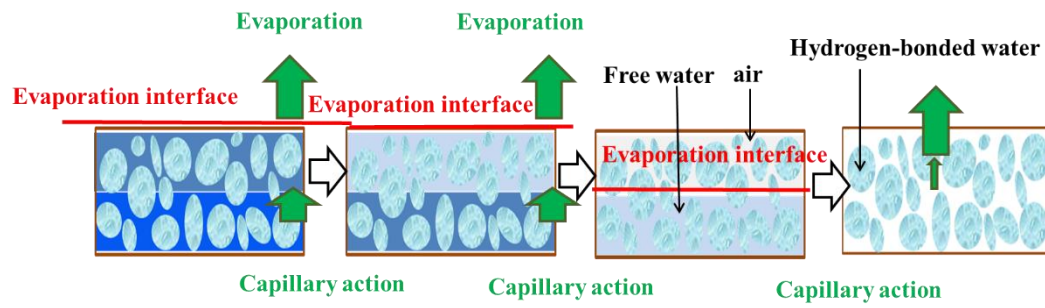


Fig. 5.10 Water-evaporation process image.

5.3.2 Evaporation Process over Time in the Short-Time Drying using the Heating-system

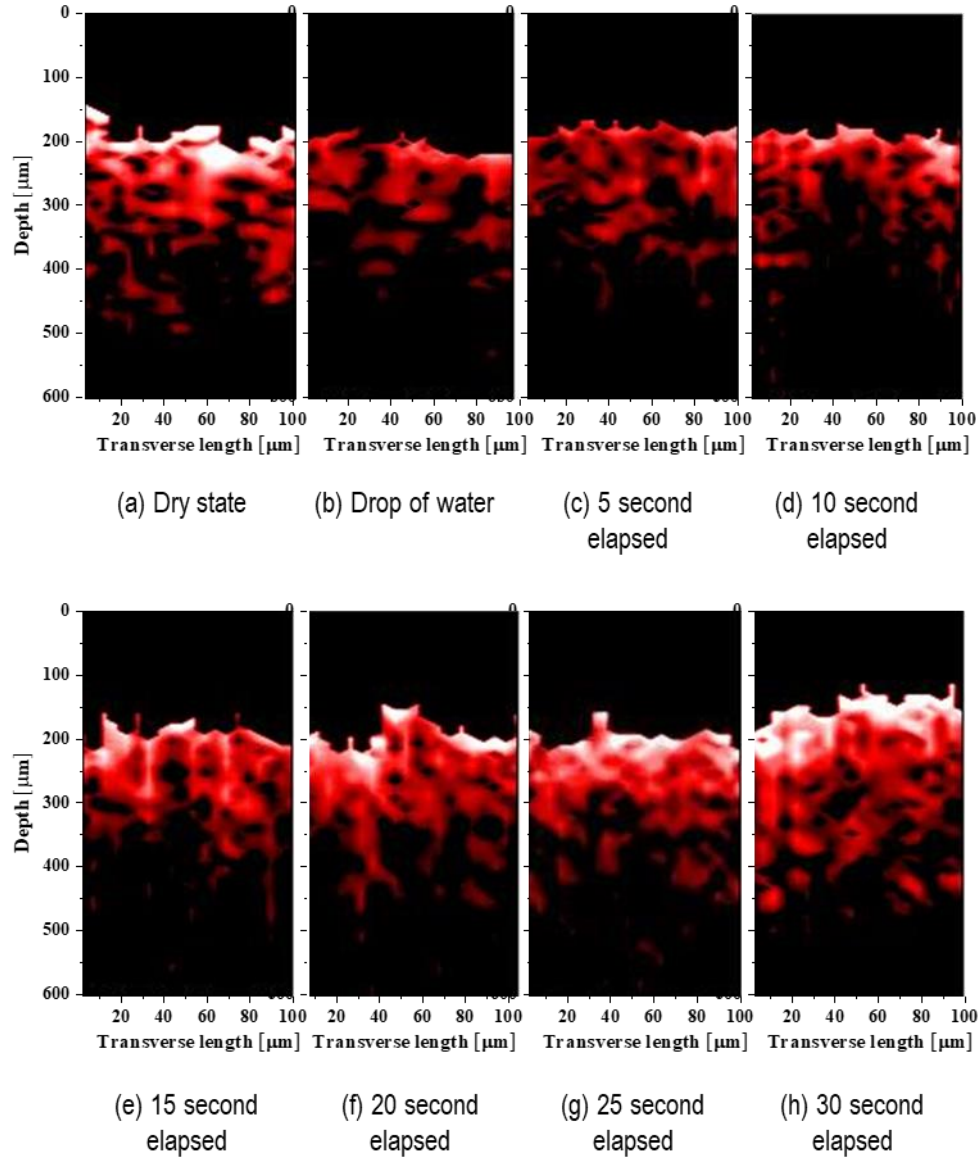


Fig. 5.11 Cross-sectional images of the sheet of compressed dry leaves from the time when water is dropped up to 30 s. The wavelength of the illuminating light is 1470 nm.

The cross-sectional images of the sheet of compressed dry leaves were acquired in the dry state at every 5 s from the time when water was dropped up to 30 s elapsed. Figure 5.11 shows the cross-sectional images for illuminating lights with the central wavelength

of 1470 nm.

It was confirmed that the brightness of the tomographic image was generally high in the dry state, whereas that in the water filling state decreased significantly. Further, the brightness increased with time. This result is similar to that of natural drying, indicating that changes in the tomographic image owing to evaporation of water contained in the sample could be confirmed even in real-time measurement.

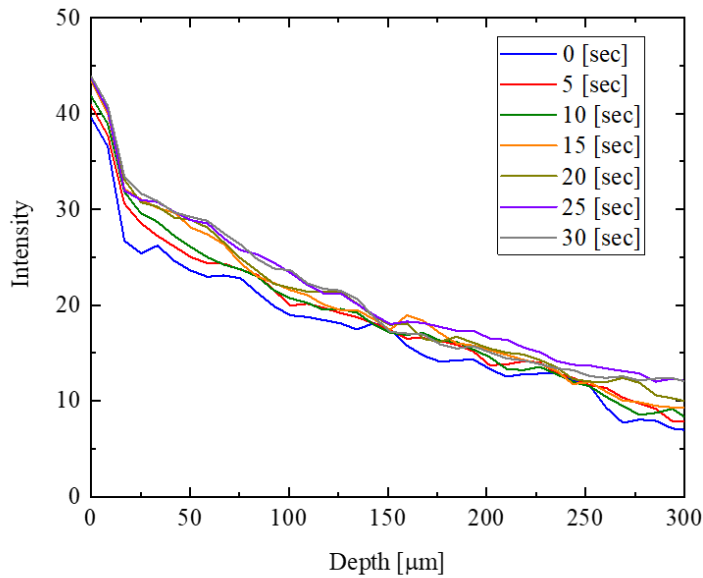


Fig .5.12 Distribution of averaging backscattered light intensity with depth as a variable.

Figure 5.12 shows the average backscattered light intensity distribution with depth as a variable calculated from the tomographic image, which was confirmed to be similar to natural drying.

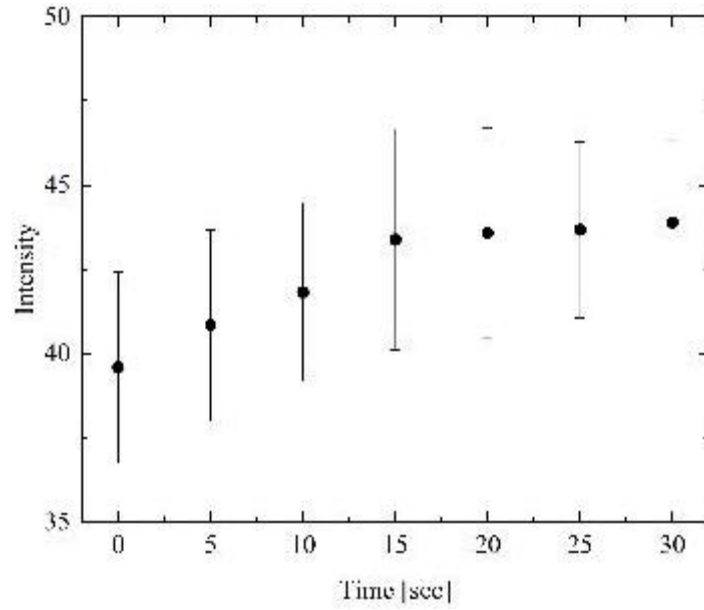


Fig. 5.13 Temporal variations of the surface intensities. The surface intensity variations are normalized by the intensities in the dry state.

Figure 5.13 shows such the variations of the surface intensity shown in Fig. 5.12 as a function of the elapsed time. The intensity variations were normalized by the intensities in the dry state. Similar to that shown in Fig. 5.8, the normalized surface intensity yielded minimum values at the time when water was dropped. This may be attributed to the refractive-index matching occurring in the state filled with water and the backscattered light becoming weak.

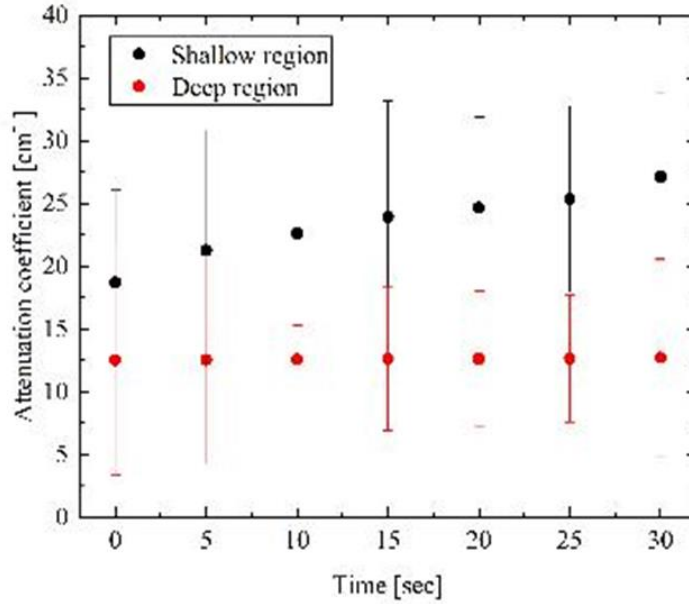


Fig. 5.14 Time course of attenuation coefficient inside the sample.

Figure 5.14 shows the time course of attenuation coefficient inside the sample. The attenuation coefficient changed in a different manner from that of natural drying in both the shallow and deep regions. In the shallow region of the sample, the attenuation coefficient increased almost constantly from immediately after the dropping of water to up to 30 s. This indicates that the water content in the shallow region decreased and the equivalent scattering coefficient increased. Whereas, in the deep region of the sample, the attenuation coefficient exhibited minimal change from immediately after the dropping of water to up to 30 s. This indicates that the amount of water in the deep region underwent minimal change. Thus, based on these results, the drying process in the sample is discussed.

Figure 5.15 shows the water-evaporation process image. The moisture in the sample was accumulated in the deep region immediately after the water was dropped. In shallow regions, the water content continued to decrease over time, which is different from the phenomenon of natural drying. As the evaporation rate of water is faster than that of water supplied by capillary phenomenon, it is considered that the drying of the surface was advanced. In the deep region, the change in water content was small even after the elapsed time, which is different from the phenomenon of natural drying. Owing to the supply of water by capillary phenomenon being slow, it is considered that water remained in a deep region. Thus, based on the above result, the possibility of a technique that can visualize the evaporation process in the biological tissue using the OCT and Beer-Lambert law was verified. Further, the possibility of a technology that can visualize the evaporation process in the biological tissue in real-time using the technique that combined the OCT and Lambert-Bell was verified.

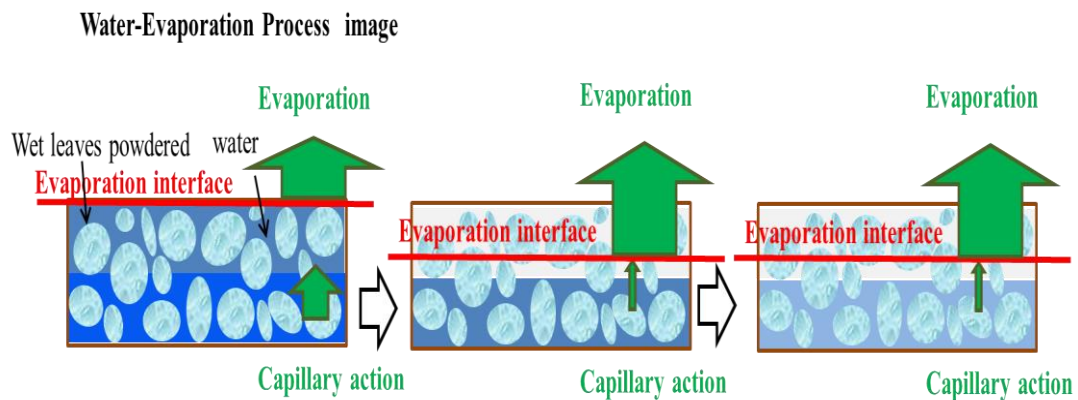


Fig. 5.15 Water-evaporation process image.

5.4 Conclusions

This Chapter proposed a method for visualizing the evaporation process of water in a dense medium. Two evaporation processes were evaluated using a combination of the near-infrared SD-OCT system and the Beer-Lambert law. In the natural drying process, the observation distribution of the moisture cloth image of shallow region and deep region of the sample was established. Whereas, in the short time drying using the heating system, the continuous imaging was verified, and the possibility of the visualization of the evaporation process of the water was demonstrated.

Chapter 6

Development of Faster SD-OCT System using Time-Stretch Spectroscopy

6.1 Introduction

In Chapter 5, the continuous imaging was verified for the short time drying process using the heating system, and the possibility of the visualization of the evaporation process of the water was demonstrated. Furthermore, it is necessary to improve the resolution of the A-scan and increase the number of measurement points due to improve the performance of the observation of water evaporation at the evaporation interface. To increase the number of measurement points, it is necessary to improve the A-scan rate. The improvement of the A-scan rate was examined. This Chapter present the development and experimental verification of a high-speed SD-OCT measurement method that enables dynamic acquisition of local water distribution changes in a tissue and three-dimensional image capture. This method is also applicable to observation of structural alterations. Similar to that in case of SD-OCT, the developed TS SD-OCT method is a technique that can detect the interference signal of the wavelength spectrum and obtain the information of the depth direction of the measurement sample via Fourier inverse transforms. SD-OCT uses a spectrometer that requires mechanical scanning for spectroscopy; however, TS SD-OCT can realize high-speed wavelength spectrum measurement using the TS-DFT technique for spectroscopy. Further, the measurement speed of this method is equal to the repetition frequency of ultrashort pulse light, and spectroscopic measurements can be conducted in the range of several tens of MHz to GHz.

TS-DFT is a method that converts a short pulse into a chirp pulse by propagating an ultrashort pulse light in a high dispersion medium such as an optical fiber, detects the chirp pulse waveform using a high-speed photodetector and a real-time oscilloscope, and then measures the spectrum of each pulse. In this method, the conversion from a time axis to a wavenumber axis and the measurement of group delay and chirp rate are required. In Ref. [59], the group velocity dispersion was measured using an expensive device, that is, an optical spectrum analyzer, before measuring the sample; subsequently, the wavelength was calibrated. However, in SD-OCT using TS-DFT, measuring both the spectrum and spectral interferogram is necessary. In Ref. [60], a single interferogram was used to calibrate and correct the nonlinearity of the chirp rate. Recently, we proposed an approximate calculation method that does not require expensive equipment and applied this method to TS-DFT [61]. This unique calculation method is referred to as applied TS-DFT micrometer length measurable light detection and ranging (MicroLiDAR) [61]. The MicroLiDAR technique has not been applied to the in-process measurement of keyholes.

In this Chapter, we constructed the TS SD-OCT that operates at an A-scan rate of 10M A-scan/s, and performed basic performance verification using a mirror as a sample. Further, as a demonstration experiment, it was introduced as a monitoring device of the laser welding process, and the possibility of continuous measurement was examined.

6.2 Procedure for calculating the distance using the approximation method

We describe a procedure for calculating the distance using the approximation method [61]. Figure 6.1 shows the procedure, which can be divided into two main parts: calibration and measurement. In the calibration part, Fig.6.1(a) shows the time series data ($Sa(T)$) measured using an oscilloscope under the condition that the difference between the reference and measurement path lengths (Δl) is Δl_1 . In this case, the wavenumber monotonically decreases as the time increases. To synchronize the increasing direction of the time axis and that of the wavenumber axis, the time axis inverted timeseries, $Sa(T')$, is calculated Fig.6.1(b)). On adding a time shift (T_0) to $Sa(T')$, the origin of the $S(T' - T_0)$ coincides with the central wavelength (Fig.6.1(c)). The Hilbert transformation of $S(T' - T_0)$ affords its real and imaginary parts (Fig.6.1(d)) from which the phase timeseries can be obtained (Fig.6.1(e)). The phase data are approximated using a quadratic curve (Fig.6.1(f) and (g)). The approximation equation is

$$\varphi(T) = B_2 T^2 + B_1 T, \quad (6.1)$$

where $\varphi(T)$ represents the phase data; T denotes time; and B_1 and B_2 represent the first and second coefficients, respectively. The several B_2 and B_1 coefficients are measured by changing Δl from Δl_2 to Δl_4 . By plotting the dependence of B_2 on Δl , the approximated line is obtained. The approximated line about B_1 is also obtained as follows:

$$B_2 = a_2 \Delta l + b_2, \quad (6.2)$$

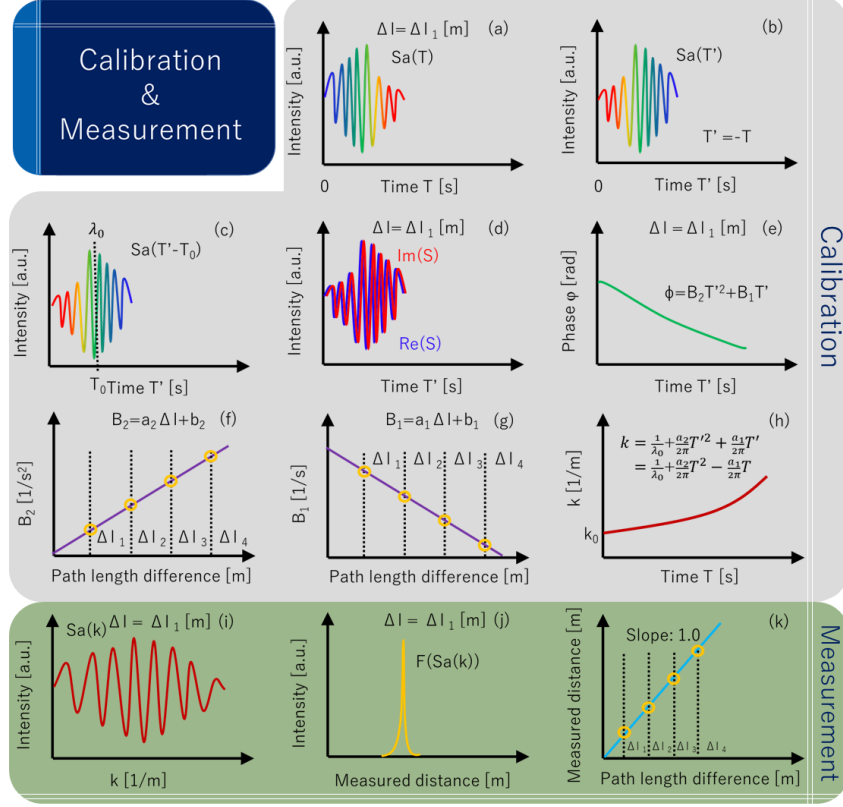


Fig.6.1 Calibration and measurement procedure: (a) original measured waveform ($Sa(T)$: time series of the waveform, Δl : path length difference, Δl_1 : first path length difference, T : time), (b) time-reversal of $Sa(T')$ (T' : reversed time), (c) time shift for the origin setting (T_0 : shifted time, λ_0 : center wavelength), (d) Hilbert converted waveform ($Re(S)$: real part of the sample, $Im(S)$: imaginary part of the sample), (e) phase time series (B_2 [$1/s^2$]: coefficient of T^2 , B_1 [$1/s$]: coefficient of T), (f) B_2 dependence on the path length difference (a_2 : coefficient of Δl , b_2 : constant), (g) B_1 dependence on the path length difference (a_1 : coefficient of Δl , b_1 : constant), (h) k dependence on time (k_0 : center wavelength), (i) measured waveform dependent on k , (j) Fourier transformation of $S(k)$ ($F(S(k))$: Fourier-transformed $S(k)$), and (k) measured distance dependence of Δl .

$$B_1 = a_1 \Delta l + b_1 \quad (6.3)$$

Where a_1 and a_2 denote coefficients. The time axis of the signal can be converted into the wavenumber with these coefficients (Fig.6.1(h)), as follows:

$$k = 1/\lambda_0 + \frac{a_2}{2\pi} T^2 - \frac{a_1}{2\pi} T \quad (6.4)$$

where λ_0 is the center wavelength of $S(t)$. Note that the relationship between Δy and Δl is $\Delta y = \Delta l/2$ when the path difference in the reference path is Δy [m].

The next section presents the measurement procedure. The time axis of arbitrary $S(t)$ is converted into a wavenumber axis with Eq. 11 (Fig.6.1(i)). Employing the Fourier transformation of $S(k)$, the horizontal axis is changed to reflect the distance (Fig.6.1(j)). The peak position of $S(k)$ indicates the measured distance. The peak position of $S(k)$ dependence on Δl is theoretically determined to be 1.00. By calculating this dependence, the calibration can be evaluated (Fig.6.1(k)).

For the practical application of the MicroLiDAR, the relationship between the measurement range, resolution, and repetition rate is explained. The measurement range is proportional to the bandwidth and chirp rate of the detector. The resolution is inversely proportional to the wavelength bandwidth of the incident light. To improve the performance of the MicroLiDAR in terms of resolution and measurement range, an incident light with a wide bandwidth and a time stretcher with a large chirp rate are necessary. The restriction condition of the repetition rate is the use of chirped pulses that do not overlap. Employing a laser source with a center wavelength of 1550 nm, wavelength bandwidth of 100 nm, repetition rate of 10 MHz, and chirp rate of 1000 ps/nm, the measurement resolution and range were calculated to be 10 μm and 40 mm, respectively.

6.3 Experimental setup and method

The experimental setup of the MicroLiDAR system is shown in Fig. 6.2. This system comprises two sections: the MicroLiDAR and welding head sections.

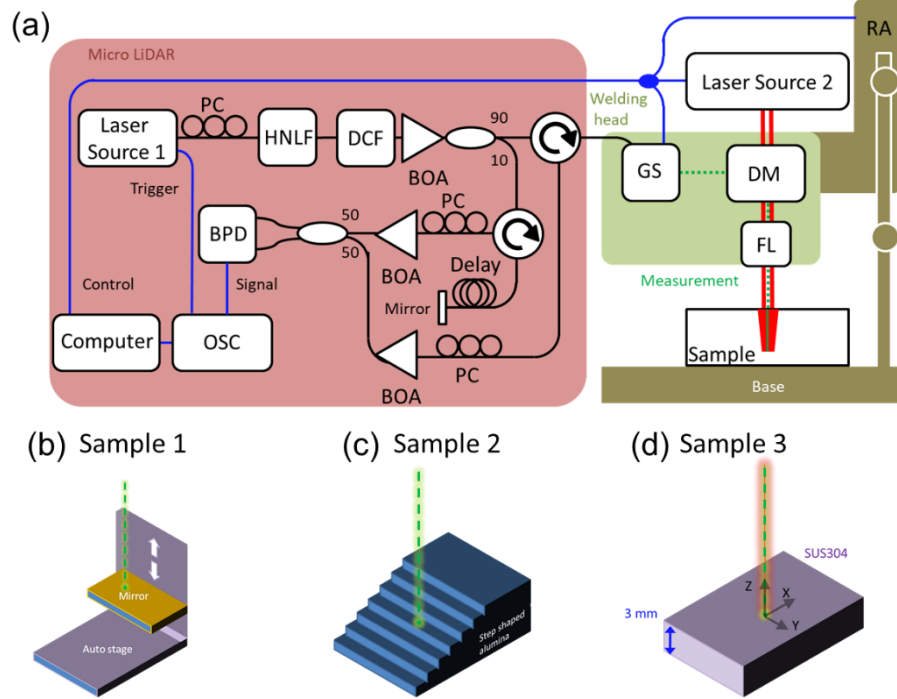


Fig.6.2. (a) MicroLiDAR and welding head (BOA, wideband optical amplifier; BPD, balanced photodetector; HNLf, highly nonlinear fiber; Laser Source 1, femtosecond laser; Laser Source 2, high-power laser; OSC, oscilloscope; RA, robot arm, (b) sample 1 (mirror with an auto stage for displacement control), (c) sample 2 (step-shaped alumina bulk), and (d) sample 3 (stainless-steel plate).

Laser source 1 is a figure-eight laser with polarization-maintaining fibers. The configuration is similar to those in Ref. [61]. The repetition rate of the output was 28 MHz, the average peak power was 6 dBm, and the nonreputational phase shifter was used as the self-starting device of the femtosecond pulse. Its center wavelength was 1550 nm, the pulse width was 400 femtosecond, and a 100-m-long highly nonlinear fiber (HNLf) was used to increase the wavelength range of the pulse. A 20-km-long dispersion-

composed fiber was used as a pulse-stretching device. The dispersion coefficient was 935 nm/s. The output of laser source 1 was amplified using a broadband semiconductor optical amplifier (BOA) after stretching in the DCF. The output was divided into two parts: one was used as the measurement light and the other as the reference light. The measurement light was launched toward the sample after adjusting its beam angle. The reflected light from the sample was coupled with the reference light, whose beams were amplified with the BOA. The beat signal was converted into an electrical signal using a balanced photodetector. The electrical signal was analyzed using an oscilloscope controlled through a personal computer. The sampling ratio of the oscilloscope was 20 GS/s, which corresponding to 7 GHz. The polarization state of the reference signal was optimized using a polarization controller to maximize the beat signal. The length of the reference light was optimized with a delay line comprising a silica single-mode fiber. The wavelength of laser source 2 was 1070 nm, which is 0.67 times higher than that of laser source 1. The peak-pulse power was 8 kW. The light was coupled with the output of laser source 1 in the dichroic mirror. Then the mixed light launched toward the sample after passing focus lens. The focus point was set to the surface of sample with 0.0345 mm spatial resolution. The laser spot diameter was 0.200 mm. The beam direction was controlled with a robot arm, which had three-dimensional freedom. A welding speed was 3 m/min. No shield gas was used. A mirror with an auto stage for controlling the position of the mirror was prepared as sample 1 (Fig.6.2(b)). The displacement was changed from 0 μ m to 40 μ m with 10- μ m steps using an ultrasonic vibration motor. Thereafter, a step-shaped aluminum bulk sample was prepared as sample 2 (Fig. 6.2(c)). The step interval was 1.0 mm, with five steps in total. A steel plate with a width of 3 mm (SUS304) was employed as sample 3 (Fig. 6.2(d)).

6.4 Experimental Result and Discussions

After the evaluation of the MicroLiDAR system, we measured the keyhole in sample 3 using a laser-welding system including the MicroLiDAR. First, we evaluated the spatial resolution of the MicroLiDAR system. The position of the mirror on the auto stage was fixed to zero point. Subsequently, the interference signal was obtained.

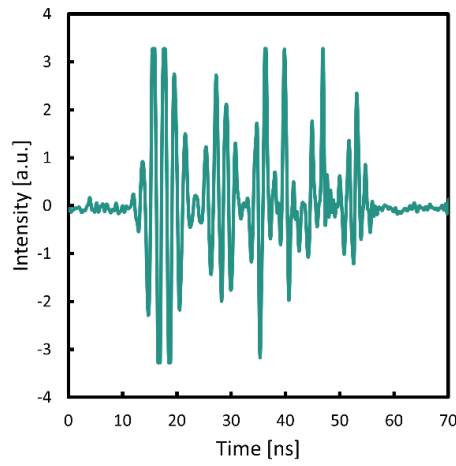


Fig. 6.3. Measured time series of the interference.

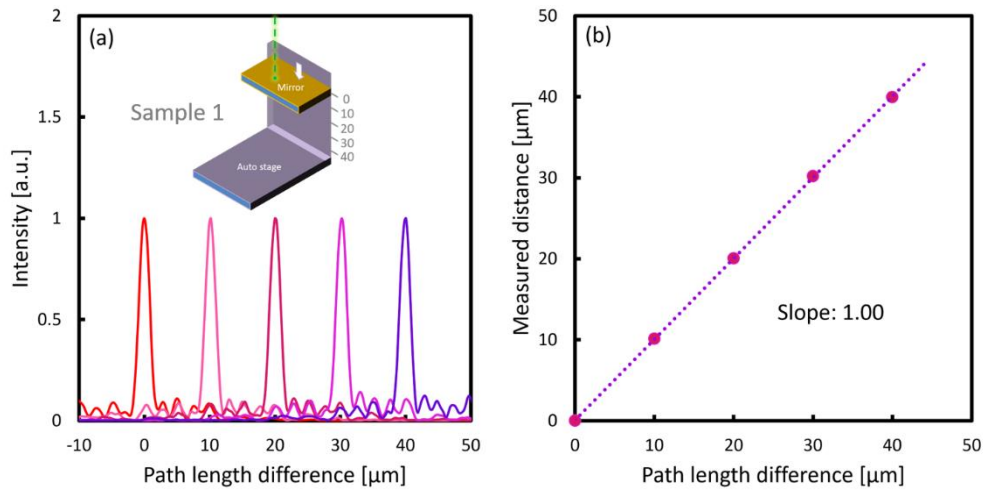


Fig. 6.4. Evaluation of the spatial resolution: (a) frequency domain analysis and (b) distance measurement.

The signal is shown in Fig. 6.3. The pulse width of the signal was 40 ns. The pulse shape was complex owing to the HNLf effect, which can be controlled using HNLfs

with different β_3 values [62]. The position of the mirror was swept from zero point to 40 μm per 10 μm . The Fourier-transformed signal is shown in Fig 6.4(a). Each peak is clearly observed. Fig 6.4(b) shows the dependence of the measured distance on the position of the mirror. The dependence was almost linear with a coefficient of 1.00, and the accuracy of this measurement was 0.21 μm ; thus, it could be applied for practical keyhole measurements. Further, the measurement range was evaluated. The laser output was swept on sample 2. The Fourier-transformed signal is shown in Fig 6.5(a). A difference of less than 5.0 mm in the distance was clearly detected. The dependence of the measured distance on the fixed distance in each step was linear, with a coefficient of 1.00, as shown in Fig 6.5(b).

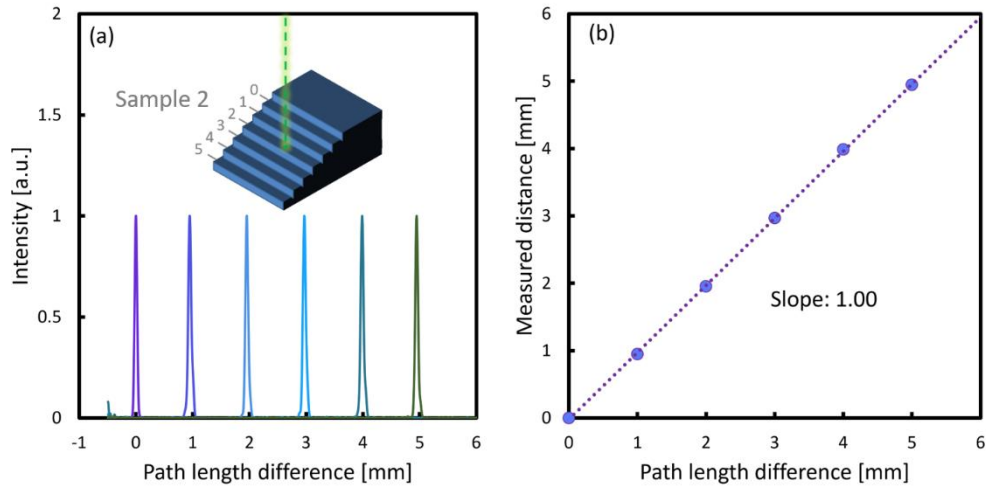


Fig. 6.5. Evaluation of the measurement range: (a) frequency domain analysis and (b) distance measurement.

Finally, we demonstrated the in-process measurement of the keyhole using a laser-welding system equipped with the MicroLiDAR. Simultaneously, the output of laser source 2 was launched toward sample 3, and the output of the MicroLiDAR was swept

around sample 3 by controlling the Galvano mirror. The output of laser source 2 was launched in the $-X$ direction at 0.05 m/s using a robotic arm. The sweeping speed of the Galva's mirror for laser source 1 was set to 18 m/s. The data at a distance of 3.6 mm were acquired during 200 μ s. The sampling step was set to 640 nm.

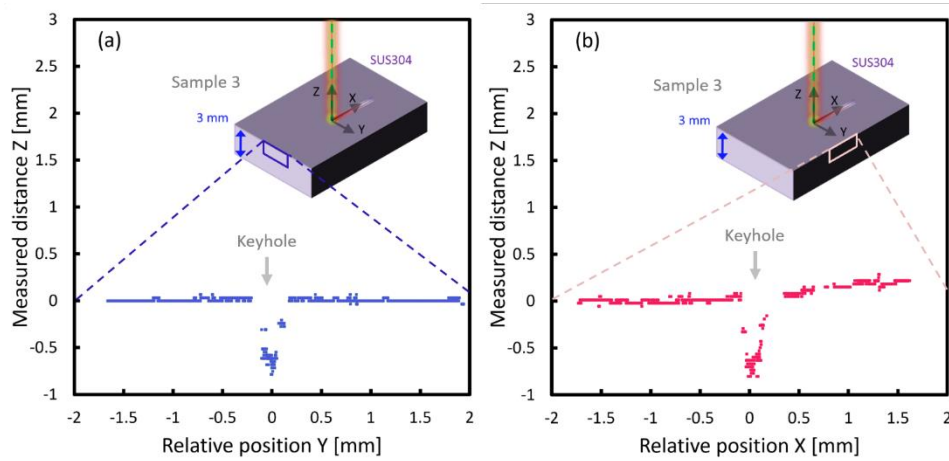


Fig. 6.6. Measured shape of the keyhole: (a) the cross-sectional area and (b) side-view dimension.



Fig. 6.7. A metallographic cross-section image of the keyhole

Fig. 6.6(a) and 6.6(b) were obtained when the measurement light was manipulated in the direction of the weld progression (cross section of the keyhole) and its perpendicular direction (side section of the keyhole), respectively. The width of the cross section of the keyhole was 0.42 mm, and the depth was 0.78 mm. Scattering signals were detected at points with the relative positions of -0.07 and $+0.12$ mm, attributable to the scattered light from the evaporated metal. Fig 6.6(b) shows that the width of the side of the keyhole was 0.46 mm, and the depth was 0.78 mm. It had almost the same dimensions as the cross section of the keyhole. Moreover, a slope was present in the range of 0.39–1.6 mm; this could be considered a molten pool. Some measurement points in this range were missed due to the weak reflected signal. As imaging analysis, we acquired the metallographic cross-section image of keyhole in Fig.6.7. The welding depth of the keyhole was measured to be 0.81 mm, which was the almost same as that of measurement value with the MicroLiDAR.

Here, we discuss the accuracy and precision of the MicroLiDAR for the surface measurement by obtaining the shape of an artificial ellipse-shaped keyhole in Fig. 6.8.



Fig.6.8. The artificial keyhole with a 0.940 mm depth, a 0.317 mm MDXD, and a 0.316 mm MDYD as true values.

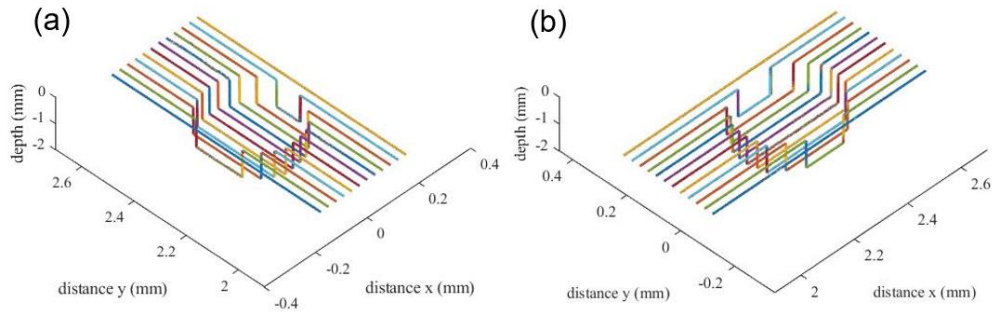


Fig. 6.9. Measured shape of the artificial ellipse-shaped keyhole: (a) y direction and (b) x direction.

The keyhole has a 0.940 mm depth, a 0.317 mm major diameter along X direction (MDXD), and a 0.316 mm minor diameter along Y direction (MDYD) as true values, which was measured with an optical microscope. We measured shape of the artificial ellipse-shaped keyhole with three times with the MicroLiDAR. The three-dimensional plotted shape of the keyhole in first acquisition was shown in Fig. 6.9. All measured value and true values were expressed in a table 6.1.

Table 6.1. Shape of an artificial ellipse-shaped keyhole and its true value.

	True value	1 st measured value	2 nd measured value	3 rd measured value	Averaged value	Standard deviation value
Major diameter along X direction (MDXD) [mm]	0.317	0.337	0.335	0.336	0.336	0.001
Major diameter along Y direction (MDYD) [mm]	0.316	0.315	0.315	0.315	0.315	0.000

In Table 6.1, the averaged value of MDXD was +0.019 mm larger than the true value of the same direction. The averaged value of MDYD was -0.001 mm larger than its true

value. These differential values were related with accuracy of the MicroLiDAR for the surface measurement. The standard deviation values of all direction were less than 0.001 mm, which was the precision of the MicroLiDAR for the surface measurement.

6.5 Conclusion

We developed a high-speed SD-OCT system using TS-DFT technology and achieved SD-OCT measurements of 10M A-scan/s. Furthermore, the degradation of sensitivity and resolution is improved by the proposed method to correct the effect of higher-order dispersion. The in-process measurement of a keyhole using a high-repetition-rate low-coherence interferometer was demonstrated. The interferometer had a repetition rate of 10 MHz and a center wavelength of 1550 nm. Its absolute spatial resolution and measurement range were evaluated to be 10 μm and 5 mm, respectively. Using the interferometer, we measured a keyhole created on a 3-mm-thick stainless-steel plate via a high-power laser with a center wavelength of 1070 nm and a peak power of 8 kW. The cross-sectional area of the keyhole was measured to be 0.42 mm \times 0.78 mm (width \times depth) using the interferometer, and its side-view dimension was 0.46 mm \times 0.78 mm (width \times depth). These findings will facilitate the development of high-performance laser-welding systems.

Chapter 7

Conclusions

The observation of distribution technique, which combined OCT using near infrared low coherence light source and Lambert-Beer law was used, and the water content imaging in the organization was verified. In addition, we demonstrated the possibility of observing water distribution and dynamic visualization of the water evaporation process.

In Chapter 1, the background and purpose of this study and composition of this paper were described. It was explained that the OCT method had recently advanced from the tomographic imaging technology to the new stage to the observing distribution technology.

The necessity of observation of distribution and dynamic visualization of water evaporation process tin conjunction with the dynamic imaging and observation of distribution of water content localized in biological tissue, and the analysis, which combined OCT and Lambert-Beer's law to enable them, were described.

In Chapter 2, the principle of OCT was described. On the Michelson interference system, which was the basis of the interferometry, the interference signal by the Michelson interferometer, the laser light source, was used and the interference signal by the low coherence Michelson interferometer when the low coherence light source as a principle of the OCT measurement was used, were described. In addition, TD-OCT and SD-OCT used in this study were described.

In Chapter 3, we verified the application of OCT to the Lambert-Beer law, which is the basis of this study. The theoretical value of the attenuation coefficient of the phantom

using the Mie scattering theory was calculated considering three definitions and compared with the OCT measurement value. Consequently, it was demonstrated that the sum of the OCT measurement value equivalent scattering coefficient and the absorption coefficient, that is $\mu_t = \mu'_s + \mu_a$ was the optimal case.

In Chapter 4, the two-wavelength OCT system was verified by measuring the stem of celery, which has a high-water content and few scatterers. It was confirmed that the change in the amount of water measured by the weigh meter and the change in the difference between the attenuation coefficients of the two wavelengths acquired via this system were similar. Based on these results, we demonstrated the water content imaging in plant tissues with this system.

Next, the possibility of measuring a high-density medium such as a living body was verified. The tissue was created by compressing the leaves of dried and powdered plants. We detected changes in the attenuation coefficient owing to the water state in the two areas of the surface and deep regions of the sample. Consequently, it was confirmed that in a high-density medium with a high refractive-index, absorption is not accumulated owing to the lack of space in the tissue filled with free water, and thus scattering is dominant. This result showed that dynamic image of water content can be realized with 1470 nm OCT alone.

In Chapter 5, we propose a method for visualizing the evaporation process of water in a dense medium. Two evaporation processes were evaluated using a combination of the near-infrared SD-OCT system and the Lambertian Beer's law. In the natural drying process, the observation of the moisture cloth image of the shallow and deep regions of the sample was established. In the short time drying process using the heating system, continuous measurements were performed, and real-time water distribution image and

observation of the evaporation process, possibility of the visualization technique were verified.

In Chapter 6, we considered the faster SD-OCT measurements system. We developed a high-speed SD-OCT system using TS-DFT technology and achieved SD-OCT measurements of 10M A-scan/s. Furthermore, the degradation of sensitivity and resolution was improved when employing the proposed method to correct the effect of higher-order dispersion.

The in-process measurement of a keyhole using a high-repetition-rate low-coherence interferometer was demonstrated. The interferometer had a repetition rate of 10 MHz and a center wavelength of 1550 nm. Its absolute spatial resolution and measurement range were evaluated to be 10 μm and 5 mm, respectively. Further, using the interferometer, we measured a keyhole created on a 3-mm-thick stainless-steel plate via a high-power laser with a center wavelength and peak power of 1070 nm and 8 kW, respectively. Consequently, the cross-sectional area of the keyhole was measured to be 0.42 mm \times 0.78 mm (width \times depth) using the interferometer, and its side-view dimension was 0.46 mm \times 0.78 mm (width \times depth). These findings are expected to facilitate the development of high-performance laser-welding systems.

Throughout the study, it was concluded that OCT could be a very practical and useful tool for visualizing and analyzing natural phenomena that have never been observed before.

References

- [1] Hans Lambers, and Rafael S. Oliveira, “Plant Water Relations,” *Plant Physiological Ecology*, pp187-263 (2019).
- [2] Tomoko M Nakanishi, and Masashi Matsubayashi, “Nondestructive water imaging by neutron beam analysis in living plants,” *Plant Physiology* 151(4), pp 442-445 (1997).
- [3] Hachiro. T, Masatoshi. O, Keiji. I, Yuko. K, Mizuho. y, Amada, and Bunjiro. I, “Evaluation of the Skin Surface Hydration in Vivo by Electrical Measurement,” *Journal of Investigative Dermatology* 75(6), pp 500-507 (1980).
- [4] J-C Tsai, C-Yu Lin, H-M Sheu, Yu-Li Lo, and Ying-Hsuan Huang, “Noninvasive Characterization of Regional Variation in Drug Transport into Human Stratum Corneum in Vivo,” *Pharmaceutical Research* 20(4), pp 632–638 (2003).
- [5] B. W. Barry, H. G. M. Edwards, and A. C. Williams, “Fourier transform Raman and infrared vibrational study of human skin: Assignment of spectral bands,” *Journal of Raman Spectroscopy* 23(11), pp 641-645 (1992).
- [6] Peter J. Caspers, Gerald W. Lucassen, Elizabeth A. Carter, Hajo A. Bruining, and Gerwin J. Puppels, “In Vivo Confocal Raman Microspectroscopy of the Skin: Noninvasive Determination of Molecular Concentration Profiles,” *Journal of Investigative Dermatology* 116(3), pp 434-442 (2001).
- [7] Dirk J. Faber, and Ton G. van Leeuwen, “Optical Coherence Tomography,” *Optical-Thermal Response of Laser-Irradiated Tissue Second Edition* 18, pp 713-742 (2011).

- [8] A. F. Fercher, C. K. Hitzenberger, and T Lasser, "Optical coherence tomography-principle and application," Rep. Prog. Phys. 66, pp 239-303 (2003).
- [9] J. M. Schmitt, A. Knüttel, and R. F. Bonner, "Measurement of optical properties of biological tissues by low-coherence reflectometry," Applied Optics 32(30), pp 6032-6042 (1993).
- [10] Joseph A. Izatt, and Michael A. Choma, "Theory of Optical Coherence Tomography," Optical coherence tomography, pp 47-72 (2008).
- [11] E. A. Swanson, J. A. Izatt, M. R. Hee, D. Huang, C. P. Lin, J. S. Schuman, W. G. Puliafito and J. G. Fujimoto, "In vivo retinal imaging by optical coherence tomography," Opt. Lett 18(21), pp 1864-1866 (1993).
- [12] Y. Takahashi, M. Iwaya, Y. Watanabe, and M. Sato, "Optical probe using eccentric optics for optical coherence tomography," Optics Communications 271(1), pp 285-290 (2007).
- [13] M. Ohmi, M. Tanigawa, Y. Wada, and M. Haruna, "Dynamic analysis for mental sweating of a group of eccrine sweat glands on a human fingertip by optical coherence tomography," Skin. Res. Technol. 18(3), pp 378-383 (2012).
- [14] 黒川隆志, 小畑秀文, 演習で身につくフーリエ解析, 共立出版株式会社 (2011)
- [15] S. H. Yun, G. J. Tearney, B. E. Bouma, B. H. Park, and J. F. de Boer, "High-speed spectral-domain optical coherence tomography at 1.3 μm wavelength," Optics Express 11(26), pp 3598-3604 (2003).
- [16] S. H. Yun, G. J. Tearney, J. F. de Boer, N. Iftimia, and B. E. Bouma, "High-speed optical frequency-domain imaging," OPTICS EXPRESS 11(22),

pp 2953-2963 (2003)

- [17] D. R. Solli, J. Chou, and B. Jalali, “Amplified wavelength–time transformation for real-time spectroscopy,” *Nature Photonics* 2, pp 48-51 (2008).
- [18] K. Goda, D. R. Solli, K. K. Tsia, and B. Jalali, “Theory of amplified dispersive Fourier transformation,” *Phys. Rev.* 80(4), pp 04821(1)-04821(12) (2009).
- [19] P. V. Kelkar, F. Coppinger, A. S. Bhushan, and B. Jalali, “Time-domain optical sensing,” *Electron. Lett.* 35(19), pp 1661-1662 (1999).
- [20] K. Goda, and B. Jalali, “Dispersive Fourier transformation for fast continuous single-shot measurements,” *Nature Photonics* 7(2), pp 102–112 (2013).
- [21] K. Goda, K. K. Tsia, and B. Jalali, “Serial time-encoded amplified imaging for real-time observation of fast dynamic phenomena,” *Nature* 458(7242), pp 1145–1149 (2009).
- [22] Keisuke Goda, Ali Fard, Omer Malik, Gilbert Fu, Alan Quach, and Bahram Jalali, “High-throughput optical coherence tomography at 800 nm,” *Optics Express* 20(18), pp 19612-19617 (2012)
- [23] P. J. L. Webster, L. G. Wright, Y. Ji, C. M. Galbraith, A. W. Kinross, C. Van Vlack, and J. M. Fraser, “Automatic laser welding and milling with in situ inline coherent imaging,” *Opt. Lett.* 39(21), pp 6217-6220 (2014).
- [24] S. Katayama, “Fundamentals and Details of Laser Welding,” Springer Singapore, Chapter 2.1 (2020).
- [25] S. Tani, Y. Aoyagi, and Y. Kobayashi, “Neural-network-assisted in situ processing monitoring by speckle pattern observation,” *Optics Express*, 28(18), 26180–26188 (2020).

- [26] A. Matsunawa, and V. Semak, "The simulation of front keyhole wall dynamics during laser welding, " *Journal of physics D: Applied physics*, 30(5), 798 (1997).
- [27] V. V. Semak, J. A. Hopkins, M. H. McCay, and T. D. McCay, "Melt pool dynamics during laser welding, " *Journal of Physics D: Applied Physics*, 28(12), 2443 (1995).
- [28] G. Chen, M. Zhang, Z. Zhao, Y. Zhang, and S. Li, "Measurements of laser-induced plasma temperature field in deep penetration laser welding," *Optics & Laser Technology*, 45, 551–557 (2013).
- [29] Y. Feng, X. Gao, Y. Zhang, C. Peng, X. Gui, Y. Sun, and X. Xiao, "Simulation and experiment for dynamics of laser welding keyhole and molten pool at different penetration status, " *The International Journal of Advanced Manufacturing Technology*, 112(7), 2301–2312 (2021).
- [30] T. R. Allen, W. Huang, J. R. Tanner, W. Tan, J. M. Fraser, and B. J. Simonds, "Energy-Coupling mechanisms revealed through simultaneous keyhole depth and absorptance measurements during laser-metal processing, " *Physical Review Applied*, 13(6), 064070 (2020).
- [31] J.J. Blecher, C.M. Galbraith, C. Van Vlack, T.A. Palmer, J.M. Fraser, P. J. L. Webster and T. DebRoy, "Real time monitoring of laser beam welding keyhole depth by laser interferometry," *Science and Technology of Welding and Joining*, 19(7), 560–564 (2014).
- [32] Z. Zhang, Y. Huang, R.Q. Z. Lei, and G. Wen. "Real-Time Measurement of Seam Strength Using Optical Spectroscopy for Al–Li Alloy in Laser Beam Welding." *IEEE Transactions on Instrumentation and Measurement* 70, 1-10 (2021).

- [33] P.H. Tomlins, R.K. Wang, “Theory, developments and applications of optical coherence tomography, ” J. Phys. D Appl. Phys. 38, 2519–2535 (2005).
- [34] T.Tsugita, R.Kimura, and T.Iwai, “Spectroscopic study on appearances of make-up skins using a visible RGB-LED OCT,” Skin.Res. Technol. 20(3), pp 379-384 (2014).
- [35] T.Tsugita, R.Kimura, and T.Iwai, “Optical coherence tomography using images of hair structure and dyes penetrating into the hair, ” Skin. Res. Technol 20(4), pp 389-398 (2014).
- [36] J. M. Schmitt, “Optical Coherence Tomography (OCT),” IEEE Journal of selected in quantum electronics 5(4), pp 1205-1215 (1999).
- [37] N. Hayashi, M. Hoshikawa, K. Ishii, T. Fujita, M. Kanamori, T. Deguchi, R. Nomura, H. Hasegawa, T. Makino, T. Hashimoto, H. Furukawa, and N. Wada, “In-process measurement of a keyhole using a low-coherence interferometer with a high repetition rate,” Optics Express, 29,(20), pp 32169-32179 (2021).
- [38] Aoyagi. T, “Pulse oximetry: its invention, theory, and future,” J. Anesth 17, pp 259-266 (2003).
- [39] J. M. Schmitt, and A. Knüttel, “Model of optical coherence tomography of heterogeneous tissue,” Journal of the Optical Society of America A 14(6), pp 1231-1242 (1997).
- [40] Lars Thrane, Harold T. Yura, and Peter E. Andersen, “Analysis of optical coherence tomography systems based on the extended Huygens–Fresnel principle,” Journal of the Optical Society of America A 17(3), pp 484-490 (2000).
- [41] V. Duc Nguyen, D. J. Faber, E. van der Pol, T. G. van Leeuwen, and J. Kalkman

- “Dependent and multiple scattering in transmission and backscattering optical coherence tomography,” *Opt. Express* 21(24), pp 29145-29156 (2013).
- [42] T. H. Chow, James C. Y. Kah, K. M. Tan, B. K. Ng, Sirajudeen Gulam Razul, Colin J. R. Sheppard, “Absorption effects in optical coherence tomography modeling,” *Proc of SPIE*, pp 6627-6661 (2007).
- [43] Katsuhiro Ishii, Rikiya Yoshida, and Toshiaki Iwai, “Single-scattering spectroscopy for extremely dense colloidal suspensions by use of a low-coherence interferometer,” *Optics Letters* 30(5), pp-555-557 (2005).
- [44] Katsuhiro Ishii, Toshiaki Iwai, and Shinichi Nakamura, “, Numerical analysis of a path-length-resolved spectrum of time-varying scattered light field” *J. Opt. Soc. Am. A* 25(3), pp 718-724 (2008).
- [45] Nakamichi, Y., Saeki, S., Saito, T., Hiro, T., Matsuzaki, M, “Quantitatively visualizing assay of drug delivery system using 2-color optical coherence dosigraphy,” *Transactions of the Japan Society of Mechanical Engineers Series B*, Vol.74, No.743, pp.1572-1578, 2008 (in Japanese).
- [46] Bouma, Brett E, Tearney, and Guillermo J, “Ophthalmic Surgery, Lasers and Imaging Retina,” *Handbook of optical coherence tomography* 34(1), pp 78-79 (2002).
- [47] Xin Ge, Shufen Chen, Si Chen, and Linbo Liu, “High Resolution Optical Coherence Tomography,” *Journal of Lightwave Technology* 39(12), pp 3824-3835 (2021).
- [48] Chieh-Li Chen, and Ruikang K. Wang, “Optical coherence tomography based angiography,” *Biomedical Optics Express* 8(2), pp 1056-1082 (2017).

- [49] E. Tokunaga, and T. Iwai, “Comparative study on visible-OCT imagings using a LED and a super-continuum laser with a wavelength-tunable filter,” Proc. of SPIE (2017).
- [50] Y. anuma, and T. Iwai, “RGB-spectroscopic OCT imaging using single-panel CMOS color camera,” Pro. of SPIE (2020).
- [51] Y. Nakamichi, S. Saeki, T. Hiro, M. and M. Matsuzaki, “In vivo tomographically diagnosing technique of early cancer using 2-color optical coherence dosigraphy,” Journal of Biomechanical Sci 12(2), pp 16-00591 (2017).
- [52] T. Ago, T. Iwai, and R. Yokota, “Extinction measurement of dense media by an optical coherence tomography technique,” Proc. SPIE (2015).
- [53] T. Makino, and T. Iwai, “Optical imaging of water distributed in plant tissues by dual-wavelengths spectral domain optical coherence tomography,” Optics-photonics Design and Fabrication, pp 216–217 (2018).
- [54] “Composition of Foods Raw, Processed, Prepared USDA National Nutrient Database for Standard,” United States Department of Agriculture Agricultural Research Service, National Nutrient Database for Standard Reference Release (2008).
- [55] Y. Wang, O. Merlin, G. Zhu, and Z. Kun Zhang, “A Physically Based Method for Soil Evaporation Estimation by Revisiting the Soil Drying Process,” Water Resources Research 55(11), pp 9092-9110 (2019).
- [56] E. T. Engelund, L. G. Thygesen, and S. Svenssonm, C. A. S. Hill, “A critical discussion of the physics of wood–water interactions,” Wood Science and Technology volume 47, pp 141–161 (2013).

- [57] Cesare Cejas, Jean-Christophe Castaing, Larry Hough, Christian Frétigny, and Rémi. Dreyfus, “Experimental investigation of water distribution in a two-phase zone during gravity-dominated evaporation,” *PHYSICAL REVIEW E* 96, 062908 (2017).
- [58] Peter Lehmann, Shmuel Assouline, and Dani Or, *PHYSICAL REVIEW E* 77, 056309 (2008).
- [59] S. Moon, and D. Y. Kim, “Ultra-high-speed optical coherence tomography with a stretched pulse,” *Opt. Express* 14(24), pp 11575–11584 (2006).
- [60] J. Kang, P. Feng, X. Wei, E. Y. Lam, K. K. Tsia, and K. K. Y. Wong, “102-nm, 44.5-MHz inertial-free swept source by mode-locked fiber laser and time stretch technique for optical coherence tomography,” *Opt. Express* 26(4), pp 4370–4381 (2018).
- [61] M. Hoshikawa, K. Ishii, T. Makino, T. Hashimoto, H. Furukawa, and N. Wada, “Low-coherence interferometer with 10MHz repetition rate,” *Opt. Rev.* 27(2), pp 246–251 (2020).
- [62] G. P. Agrawal, “Nonlinear Fiber Optics,” Academic Press, Chap. 3, pp 84-90 (1995).

Acknowledgment

The author is most indebted to Prof. T. Iwai for his guidance, encouragement and support, without which this work would never been started.

He gratefully acknowledges Prof. I. Nishidate, Prof. I. W. Lenggoro, Dr. N.Wada in National Institute of Information and Communications Technology (NICT), Dr. H.Furukawa in NICT, Dr. S.Shinada in NICT for their kind encouragement and useful advices.

Acknowledge is extended to Prof. Y. Takagi, Prof. K. Masuda, Prof. Y. Ueda for their helpful suggestions in writing this paper.

Cordial acknowledgement is extended to Mr. T. Ago, Mis. R. Yokota, Mr. H. Ujino and Mis. H. Ozaki for their aid and scientific attitude which they brought to this work. Hearty thanks are also extended to all laboratory members for their cooperation and for creating an enjoyable research atmosphere.

This work was partially supported by JSPS Kakenhi (Grant 20K05188) and the Moonshot R&D Program for Agriculture, Forestry, and Fisheries (BRAIN and the Cabinet Office, Japan). The authors thank Mitsuki Wada, Yousuke Asanuma, Iori Nakaya and Yuria Watanabe for their supports during the numerical simulations and experiments and JT Group for supplying the samples.

This work was partially supported by Japan Science and Technology Agency Adaptable and Seamless Technology transfer Program through target-driven R&D (JPMJTR192F). The authors thank Prof. Neisei Hayashi in Graduate School for the Creation of New Photonics Industries (GPI), Dr. Masaharu Hoshikawa in GPI, Prof. Katsuhiro Ishii in GPI

Mr. Takuma Fujita in Nadex Products Co., Ltd. Laser R&D Center, Mr. Masakazu Kanamori in Nadex Products Co., Ltd. Laser R&D Center, Mr. Takahiro Deguchi in Nadex Products Co., Ltd. Laser R&D Center, Mr. Ryo Nomura in Nadex Products Co., Ltd. Laser R&D Center, Mr. Hiroshi Hasegawa in Nadex Products Co., Ltd. Laser R&D Center, Mr. Takahiro Hashimoto in NICT for giving me the opportunity to do a useful experiment.